Revision 1

Cu isotope fractionation between Cu-bearing phases and hydrothermal fluids: insights from ex situ and in situ experiments

Dongmei Qi [a,b,c], Chao Zhang [a,c,*], Marina Lazarov [c]

[a] State Key Laboratory of Continental Dynamics, Department of Geology, Northwest University, 710069 Xi'an, China

[b] Xinjiang Key Laboratory for Geodynamic Processes and Metallogenic Prognosis of the Central Asian Orogenic Belt, Department of Geology and Mining Engineering, Xinjiang University, Urumqi 830046, China

[c] Institute of Mineralogy, Leibniz University of Hannover, Callinstrasse 3, Hannover D-30167, Germany

* Corresponding author. Email: zhangchao@nwu.edu.cn

This is the peer-reviewed, final accepted version for American Mineralogist, published by the Mineralogical Society of America.
The published version is subject to change. Cite as Authors (Year) Title. American Mineralogist, in press.
DOI: https://doi.org/10.2138/am-2023-9155. http://www.minsocam.org/

Abstract

Cu isotope ratios have been widely applied to fingerprinting metal sources, tracking fluid pathways, and tracing mineralization processes, for which knowledge of isotope fractionation is required. This paper presents new experimental calibration data of Cu isotope fractionation between Cu-bearing minerals (native Cu and cuprite) and Cl-bearing hydrothermal fluids at 25−800°C and 0.1−200 MPa. The experiments were performed either using a Teflon beaker on a hotplate, a rapid heat/rapid quench argon cold seal pressure vessel (RH/RQ Ar-CSPV), or a large volume fluid reactor, which enabled fluid sampling ex situ (the former two) and in situ (the latter). Three setups were designed to investigate Cu isotope fractionation ($\Delta^{65}Cu_{fluid\text{-}mineral}$): (1) associated with Cu(I) dissolution, Cu(I) disproportionation as well as oxidation of Cu(0) and Cu(I) in Cu±Cu_2O+HCl systems at temperatures of up to 800°C and pressures of up to 200 MPa, (2) related to Cu-Au alloying processes in the Cu+NaCl/HCl system at 600°C and 150 MPa, (3) to evaluate the influences of different sampling techniques (ex situ versus in situ) and superimposed cooling processes. The selected system is Cu_2O+NaCl+0.2 m HAc/NaAc (pH-buffer) and runs were conducted at 200-250°C and 20 MPa.

$\Delta^{65}Cu_{fluid\text{-}mineral}$ shows the least variation during solid separation from source fluids, generally less than 0.16±0.03‰. Positive $\Delta^{65}Cu_{fluid\text{-}mineral}$ values are found in most runs excluding cuprite dissolution in NaCl/HCl solutions at 200–250°C, 20 MPa, and 800°C, 200 MPa. Cu oxidative leaching into Cu(I) results in decreasing $\Delta^{65}Cu_{Cu(I)\text{-}Cu(0)}$ values from 0.12±0.05‰ to 0.07±0.05‰, and -0.30±0.03‰ at 25, 50, and 200°C, respectively. In contrast, Cu dissolution at high temperatures (600−800°C) leads to Cu(I)-containing quench fluids and subsequent native Cu precipitates. Both products are enriched in heavy isotopes by up to 5‰, caused by preferential enrichment of ^{65}Cu at the surface layer during the alloying-induced diffusion transport process.

Cuprite oxidative leaching in HCl leads to fluids enriched in Cu(II), and the corresponding $\Delta^{65}Cu_{Cu(II)-Cu(I)}$ increases from 0.52±0.04‰ at 25°C to 0.89±0.02‰ at 50°C. Fluids are enriched with light isotopes (^{63}Cu) during cuprite dissolution at 200, 250, and 800°C, i.e., 0–0.55±0.04‰ lower than the precursor. At 250−300°C, Cu(I) disproportionation into Cu(II) and Cu(0) dominates the observed isotope fractionation, yielding $\Delta^{65}Cu_{fluid-Cu2O}$ up to 0.59±0.03‰ and $\Delta^{65}Cu_{Cu(0)-Cu2O}$ up to -0.28±0.02‰.

Rapid cooling (3−25 K s^{-1}) relative to slow cooling (0.014 K s^{-1}) can cause phase separation as well as significant isotope fractionation, particularly if fluids cool from an intermediate high temperature to ambient temperature (e.g., from 200−300 to 25°C), which highlights the importance of kinetic processes that may potentially alter the isotope composition of natural ore-forming fluids.

Keywords: Cu isotope fractionation, redox reaction, cooling, Cu-Au alloying, diffusion, in situ fluid sampling.

1. INTRODUCTION

Copper (Cu) is a chalcophile and fluid-mobile element that exhibits moderately volatile behavior at high temperatures. As revealed by numerous case studies of Cu mineralization, hydrothermal fluids play a vital role in Cu sequestration, mobility, and enrichment. In ore-forming fluids, Cu is transported as a monovalent Cu(I) species, such as CuHS in low-temperature sulfidic solutions (<350°C; Crerar and Barnes 1976; Mountain and Seward 1999, 2003) and CuCl, $CuCl_2^-$ at temperatures higher than 350°C in sulfur-poor systems (Fulton et al. 2000b; Berry et al. 2006; Hack and Mavrogenes 2006; Zajacz et al. 2011; Mei et al. 2014; Schmidt et al. 2018). Cl is one of the most significant ore fluid components, for instance, high temperature (>400°C) porphyry and low temperature (<200°C) sediment-hosted ore systems contain up to 55 wt.% $NaCl_{equivalent}$ (e.g., Roedder, 1984; Hezarkhani and Williams-Jones, 1998; Ulrich et al., 1999). Experimental investigations show that aqueous Cl positively correlates to Cu content in aqueous fluids. Synthetic fluid inclusion studies demonstrate that chloride-bearing fluids transport up to 15 wt.% Cu at 525-1000°C and 150-1700 MPa (Hack and Mavrogenes, 2006; Qi et al., 2020; Zajacz et al., 2011). On the other hand, low temperature (<300°C) fluids contain up to 3 wt.% Cu (Liu et al., 2001; Xiao et al., 1998). Thus, ligands such as chloride play an important role in metal complexation as well as in ore deposit formation.

In nature, Cu isotopes provide a potential proxy for planetary as well as terrestrial processes, with an overall $\delta^{65}Cu$ value varying from -16.98 to 25.73‰ (Mathur et al. 2009; Zegkinoglou et al., 2023)). Hereafter $\delta^{65}Cu$ (‰) denotes as $[(({}^{65}Cu/{}^{63}Cu)_{sample}/({}^{65}Cu/{}^{63}Cu)_{NIST\ 976}) - 1]\times 1000$, and NIST 976 refers to the international reference material). Among these processes, hydrothermal processes can result in significant mass-dependent isotopic fractionation ($\Delta^{65}Cu_{A\text{-}B}(‰)=\delta^{65}Cu_A-\delta^{65}Cu_B$, phase A refers to fluid in most cases (to a neoformed Cu-bearing

73 solid in a few cases) and phase B refers to a Cu-bearing solid in this study). Therefore, Cu
74 isotopes provide information that furthers our understanding of hydrothermal processes, which
75 could in turn lead to greater success in the exploration for concealed orebodies as well as in
76 identifying primary or secondary ore minerals in various types of ore deposits, such as porphyry
77 deposits (Li et al. 2010; Gregory and Mathur 2017; Zheng et al. 2019; Kim et al. 2019; Kidder
78 et al. 2021), skarn deposits (Maher and Larson 2007; Wang et al. 2017), high sulfidation
79 epithermal deposits (Duan et al. 2016; Wu et al. 2017), orogenic deposits (Molnár et al. 2016;
80 Wang et al. 2018), volcanogenic massive sulfide deposits (Mason et al. 2005; Ikehata et al.
81 2011), Mississippi Valley-type deposits (MVT; Luczaj and Huang 2018), sediment-hosted Cu
82 deposits (Asael et al. 2007, 2009, 2012), vein-type deposits (Markl et al. 2006; Yao et al. 2016),
83 magmatic Ni-Cu-PGE deposits (Ripley et al. 2015; Zhao et al. 2017; Brzozowski et al. 2021),
84 native Cu deposits (Larson et al. 2003; Bornhorst and Mathur 2017), and modern seafloor black
85 smoker chimneys (Rouxel et al. 2004; Berkenbosch et al. 2015; Zegkinoglou et al., 2023), as
86 well as in the associated oceanic crust alteration processes (Huang et al. 2016a; Liu et al. 2019;
87 Zeng et al. 2021). Among them, high-temperature (hypogene) ore-forming processes can result
88 in Cu isotope variations over ~2‰ (Larson et al. 2003; Rouxel et al. 2004; Mathur et al. 2009;
89 Wu et al. 2017; Zhao et al. 2017). More pronounced variations can be induced by supergene and
90 sea-floor alteration processes, from -16.96 to 25.73‰ (Mathur et al. 2009, 2010; Kim et al.
91 2019) and from -1.52 to 4.70‰ (Maréchal et al. 1999; Zhu et al. 2000; Rouxel et al. 2004;
92 Dekov et al. 2013; Berkenbosch et al. 2015; Liu et al. 2019; Zeng et al. 2021; Zegkinoglou et al.,
93 2023), respectively. This large variation (up to 42.69‰) is due to the combined effect of various
94 controlling mechanisms, such as reductive dissolution during redox state change (Ehrlich et al.
95 2004; Pękala et al. 2011; Qi et al. 2019) and oxidative leaching (Mathur et al. 2005; Fernandez

and Borrok 2009; Kimball et al. 2009)], liquid-vapor partitioning (reaching -1‰; Maher et al. 2011; Rempel et al. 2012), mineral dissolution (Syverson et al. 2021), exsolution of hydrothermal fluids from silicate melts (Guo et al. 2020), sorption (Ijichi et al. 2018) and evaporation (Ni et al. 2021). Furthermore, theoretical calculations provide more information on knowledge of equilibrium and kinetic Cu isotope fractionation factors for different Cu species (Seo et al. 2007; Fujii et al. 2013, 2014; Sherman 2013; Sherman and Little 2020; Liu et al. 2021). These experimental and theoretical studies provide first-order constraints on understanding Cu isotope fractionation in geological systems as well as fingerprinting associated with hypogene and supergene processes.

Copper can exist in the metallic (Cu(0)), cuprous (Cu(I)), and cupric (Cu(II)) oxidation states. Interestingly, minerals that contain Cu in these three valence states can coexist in both supergene and sea-floor settings (e.g., Hannington et al., 1988; Larson et al., 2003). This paper is dedicated to understanding the partitioning of Cu isotopes among Cu(0), Cu(I), and Cu(II) in aqueous environments in a range of geological settings, e.g., near-surficial, epithermal-sedimentary, and magmatic. In this paper, we present the results of Cu and Cu_2O dissolution in HCl/NaCl solutions. Cu and Cu_2O were selected due to their important valence and abundance in geological settings, such as the supergene setting. More specifically, native Cu is an important type of copper deposit in nature, such as the world-famous Keweenaw Peninsula native copper district. Native Cu has also been observed in ultramafic and mafic rocks from ophiolitic and orogenic massifs (Zhang et al. 2006; Ikehata and Hirata 2012; Eslami et al. 2021 and references therein). Interestingly, native Cu is also found coexisting with Cu(II) minerals (e.g., atacamite, covellite) during the alteration process of chalcopyrite due to interaction with seawater at the ocean floor (Hannington et al. 1988). For example, native Cu formation is

119 suggested to occur due to (i) low-temperature in situ alteration of magmatic or hydrothermal Cu
120 sulfides at highly reducing conditions (e.g., Eslami et al. 2021), (ii) by precipitation from
121 low-temperature metamorphogenic hydrothermal fluids (e.g., Bornhorst and Mathur, 2017), or
122 (iii) during crystallization in equilibrium with mafic magma at high temperatures (e.g., Zhang et
123 al. 2006). Experiments on the dissolution and oxidation of native Cu at temperatures above
124 100°C are scarce and can have direct implications for ore-forming and magmatic-hydrothermal
125 processes. Transformations in the oxidation state and complexation of Cu are strongly dependent
126 on physical conditions, thus the mechanisms by which these transformations may affect the
127 isotope composition of fluids need to be investigated further. Despite this, natural and
128 experimental findings show that high-temperature processes can result in large variations in Cu
129 isotope composition, e.g., fractionation up to 18‰ (e.g., Busigny et al. 2018; Guo et al. 2020; Ni
130 et al. 2021), and it is unclear whether this significant degree of fractionation is related to post
131 cooling processes. In this study, we analyzed Cu isotopes of the coexisting Cu-bearing minerals
132 and hydrothermal fluids, and these data allow us to examine the dependence of Cu isotope
133 fractionation on oxidation/reduction processes and cooling rates.

134 **2. EXPERIMENTAL APPROACH**

135 All experiments and measurements in this study were carried out at the Institute of
136 Mineralogy, Leibniz University of Hannover (Germany).

137 Cu tubing (2.45 mm I.D., 2.55 mm O.D., and 30 mm length) and Au tubing (2.80 mm I.D.,
138 3.20 mm O.D., and 30 mm length) were used as capsule materials. Thin Cu foil (thickness of
139 0.05 mm) and fine copper powder (14−25 μm) were used as additional Cu(0) sources. Cuprite
140 (Cu_2O) in powder and pellet form was used as a source of Cu(I). The pellet preparation followed
141 the procedure of Qi et al. (2020). Starting solutions containing NaCl or HCl were doped with

142 400−600 μg g^{-1} RbCl and CsCl for verification of dilution levels during analyses. Equimolar
143 acetic acid and crystalline anhydrous sodium acetate were added to NaCl solution to buffer pH at
144 ca. 4.6. Although decomposition of acetate was generally found to be the dominant reaction at
145 temperatures below 400°C (Kharaka et al., 1983; Palmer and Drummond, 1986). Hydrothermal
146 studies of acetate decomposition have been carried out in stainless steel vessels (Kharaka et
147 al.,1983), Ti vessels, Au cups or bags (also used in this study), silica tubes, and Pyrex tubes
148 (Palmer and Drummond, 1986). Their results have shown that aqueous solutions of acetic acid
149 are relatively stable under thermal stress (Kharaka et al.,1983; Palmer and Drummond, 1986).
150 Our runs were performed much shorter than the half-life of acetate (half-lives of ca.300–1.2 $\times 10^5$
151 hours at 350°C; Kharaka et al.,1983; Palmer and Drummond, 1986). Due to acetate
152 decarboxylation, a pH-buffered solution was not used in high-temperature runs (≥600°C).
153 Capsule filling is shown in Fig.1c. Solid reagents were loaded before aqueous solutions.
154 Capsules were squeezed on top to remove additional air and weighed, cut, and welded shut under
155 a flow of Ar gas. To avoid volatile loss due to vaporization during welding of the upper end of
156 the capsule, the filled capsules were frozen by wrapping them in wet tissues and submerging
157 them in liquid nitrogen. The capsules were weighed before and after welding, and only those
158 without mass change were selected for the subsequent experiments. Using these experimental
159 materials, three sets of experiments with different purposes were performed at 25−800°C and
160 0.1−200 MPa (Table 1).

161 The first set of experiments (Set 1) was designed to assess Cu isotope fractionation related
162 to the dissolution of Cu(0) and Cu(I) in an HCl solution. Low-temperature runs (25−50°C) were
163 performed within one hour on a hot plate (Fig. 1a). These runs were performed for a short period
164 (1 h), to avoid vapor loss that may carry the light Cu isotope (^{63}Cu) during the heating process.

Metallic copper or cuprite pellets and aqueous HCl solutions were added to Teflon beakers which were closed tightly during the run. The oxygen fugacity of the system can be determined by the proportion of oxygen in the atmosphere. The volume percentage of O_2 in the air is 20.9476% at 15°C (Lide, 1997), and log$f$O2 is -0.68 (log$f$$O_2$=log 0.209476×1(bar)). The volume percent of O_2 is constant with temperature, and hence, log$f$$O_2$(air) is insensitive to temperature. High temperature and high-pressure experiments (200−800°C, 20−200 MPa) were conducted in RH/RQ Ar CSPV (details are given in Matthews et al. 2003). Note that the quench fluid of DQ169* is collected from a fluid inclusion synthesis experiment by Qi et al. (2020). In this run, cuprite powder, quartz cylinders, and an HCl solution were loaded into a Cu capsule. The temperature and pressure varied within ±5°C and ≤ ±5 MPa, respectively. The intrinsic oxygen fugacity imposed by a Ni filler rod in this vessel was buffered at ca. NNO + 2.3 (2.3 log units above the Ni-NiO buffer; Berndt et al. (2001)). Accordingly, log$f$$O_2$ of 200°C-800°C runs vary between -115 and -22 (Huebner and Sato, 1970). Starting materials such as Cu foil, Cu powder or cuprite pellets, and aqueous HCl or NaCl solutions were added to Au/Cu capsules (Fig. 1b). These capsules were attached to a nickel rod with a metal ring at the bottom, and then pressurized to target pressure at room temperature and held at the water circulating zone until the furnace was heated to target temperature, and quickly transferred to the heated hot zone by an outer mobile magnet. Three types of quench techniques in RH/RQ Ar CSPV runs were applied to check whether Cu isotope fractionations are affected by different cooling rates. Cooling rates of 0.5, 3, and 25 K/s refer to cooling the autoclave at room temperature, cooling the autoclave with compressed air at the hot end, and cooling the sample at the cool water zone, respectively, (more details are given in Qi et al. 2020). The final experimental products after quenching included both aqueous fluids and solid precipitates; the latter of which may be formed either at the

188 experimental condition or during quenching as a cooling product.

189 Set 2 experiments were performed to study the Cu isotope fractionation of Cu dissolution
190 and precipitation processes in a Cl-bearing solution. Cu powder and 1.5 m NaCl/HCl solutions
191 were added into Au capsules. Experiments were conducted at 600°C and 150-180 MPa in
192 RH/RQ Ar-CSPVs.

193 Set 3 experiments were conducted to investigate fluid chemistry differences sampled by ex
194 situ and in situ techniques. This series of experiments was also designed to investigate the
195 different cooling rates on the phase transformation and the associated isotope fractionation.
196 Cuprite pellets and pH-buffered NaCl solution were loaded into either an Au reaction cell (~60
197 ml) or Au capsules (similar to set 2). These runs were performed with two different vessels at
198 100−250°C, 20 MPa, i.e., a large volume fluid reactor (Cp3, 6) vs. an RH/RQ Ar CSPV (Cp4-5,
199 7-8). The large-volume fluid reactor (also called an internally filtered gold-cell reactor) was used
200 for inline fluid sampling (Fig. 1c), which is described in detail by Dickson et al. (1963) and
201 Seyfried et al. (1979). The oxygen fugacity of this device has not been determined, but it may be
202 indicated by the mineral assemblages. Qi (2019) performed runs with Cu_2O-HAc-KAc in the
203 same device. Although the solution composition of Qi (2019) is slightly different from this study,
204 the pH of solutions of 250°C runs is almost the same (4.5-5.1). Their results indicate that Cu_2O is
205 the residual phase in all runs, Cu appears at the early stage (at 7-24h) at 250°C, and CuO is
206 present at the late stage (72 h) in both 150 and 250°C runs. This may indicate that the oxygen
207 fugacity of the large-volume fluid reactor varies between Cu-Cu_2O and Cu_2O-CuO. The
208 procedure for the large-volume fluid reactor runs is as follows. The large-volume fluid reactor
209 would be heated to a target temperature within 0.5 h isobarically (e.g., 250°C). After reaching the
210 target temperature pressure will be readjusted to the target pressure. The temperature and

pressure vary within ±2°C and ≤ ±0.1 MPa, respectively. In situ solutions were extracted through a long titanium tube (ca. 25 cm), a three-way valve, and two interconnected titanium tubes and containers (total length of ca. 5cm). These titanium parts were not heated during the run so they may have a lower temperature than the internal fluid reactor. The titanium containers (~1 ml) were used to temporarily store the in situ solutions. Each sampling was done twice by opening the main valve connected to the longest titanium tube, and then opening the 1st valve to collect the first sample and closing this valve (Fig. 1c). The 2nd solution follows the same procedure. The 1st fluids represented the flush solution which may not have been well mixed and solids may precipitate along the cooled pathway. In comparison, the 2nd solution represented experimental fluid and was further processed for chemical purposes. After the run, the furnace was removed from the autoclave, and the cooling rate was about 0.014 K/s from 250°C down to 50°C. Run Cp3 was carried out at a constant temperature of 200°C for 48 h and in situ solutions of Cp3 were extracted at 200°C, 48 h, and 100°C, 50 h. Run Cp6 investigated both the heating and cooling effect on Cu content and the corresponding isotope fractionation in a temperature range of 100-250°C. In situ solutions of Cp6 were sampled at 100, 150, 200, and 250°C with a time interval of 1 h and 64 h, and along the cooling process from 250 to 100°C within 2 h. Their comparable runs Cp4-5 and Cp7-8 were performed in RH/RQ Ar-CSPVs at 200 and 250°C, respectively. However, the ex situ fluid sampled and post-run treatments of Cp4-5 and Cp7-8 are different and described below.

Fluids collected from 25−50°C experiments were processed directly in an ultra-clean lab. Quench fluids collected from capsules (Set 1, 2, Cp4-5 of Set 3) were treated via the following steps: (i) The squeezed capsules were expanded by annealing at 150°C for 15 min in a furnace at atmospheric pressure. Note that copper diffusion in gold at 150°C is very slow, and the diffusion

234 layer is less than 1.8×10^{-5} μm (4 h; Tompkins and Pinnel 1976). Thus, annealing of Au at 150°C
235 would keep the isotopic data of the capsules to remain invariant on the time scale of our
236 experiments. (ii) These capsules were opened by submerging them into liquid nitrogen and then
237 piercing them with a steel needle, which enabled almost 100% fluid recovery. However, Cp7 and
238 Cp8 of Set 3 were treated differently from Cp4 and Cp5. Capsules from Cp7-8 were pierced by
239 steel needles on a frozen stage. Both capsules were transferred to two open Teflon vials which
240 were heated at 100°C to remove all the liquid phases. After two days, the weight of the capsule
241 was stable, and the mass difference between the initial capsules and the heated capsules equaled
242 the loaded aqueous solution. Capsules were cut through to fully retrieve the solids. The solids
243 included cuprite pellets and blue precipitates. Solids were rinsed with Milli-Q water, which was
244 treated as an ex situ fluid. Au capsules were rinsed with 1 m HCl solution in an ultrasonic bath
245 for 10 minutes. Finally, all fluid samples were transferred to Teflon vials in an ultra-clean lab for
246 further chemical treatment.
247 Both the surface and the cross-section of the cuprite pellets of Cp3-6, and Cp18-19 were
248 mounted in resin for in situ analyses. The surface of reacted cuprite pellets was flat enough so
249 some precipitates remained after polishing. The separation of solids from quenched fluids was
250 first done by centrifuging. Then the fluids were passed through filters, that were rinsed with MQ
251 water to fully remove any liquid residue. Fluid samples were then evaporated on a hotplate until
252 a dry residue was obtained. Finally, solids were transferred to vials, and the filter papers were
253 pulled off. The solids retrieved were directly processed as solutions for elemental and isotopic
254 analyses.

3. ANALYTICAL METHODS

The pH values of the solutions were measured with an *InLab® Flex-Micro* pH combination electrode (*Mettler Toledo GmbH, Germany*). The pH of the fluids was measured at room temperature for both stock solutions and sampled fluids during and after the run. Standard pH solutions and each fluid sample were measured three times, and the uncertainty was the standard error.

The composition of cuprite pellets and post-experiment overgrowths of secondary minerals were determined on polished sections using a CAMECA SX100 electron probe micro-analyzer (EPMA). The reference materials for calibration included jadeite (Na), NaCl (Cl), and Cu (Cu). Raw analytical data were corrected using the standard PAP procedure (Pouchou and Pichoir 1991). Acceleration voltage was set at 15 kV. A focused beam and a 15 nA beam current were used for analyzing solid phases.

Sampled fluids were transferred into acid-cleaned Savillex PFA labware and further treated with deionized 18.0 Milli-Q water and Teflon-distilled acids (HNO_3 and HCl) in an ultra-clean lab. Collected ex situ and in situ fluids were evaporated to dryness at 90°C on a hotplate, and digested in 1 ml of 3% HNO_3 solution. Solid phases were first processed with a freshly prepared aqua regia solution and then the procedure described above was followed. Cu deposits on the Au substrate were digested by ~ 15 ml of 6 mol L^{-1} HCl at 120°C overnight. After the removal of the Au foil, the solutions were processed following the same procedure for sampled fluids.

The Cu concentration of all solutions was analyzed by inductively coupled plasma optical emission spectrometry (ICP-OES) on a Varian Vista Pro system (Varian GmbH, Germany), following the procedure of Roebbert et al. (2018). The precision of the ICP-OES analyses was better than 10 % (2SD).

For the isotopic analyses of experimental products, the potential isobaric interference between $^{31}P^{16}O_2^+$, $^{40}Ar^{23}Na^+$, $^{23}Na^{40}Ca^{+,}$ and ^{63}Cu as well as between $^{32}S^{16}O_2H^+$, $^{40}Ar^{25}Mg$, $^{48}Ca^{16}OH$, and ^{65}Cu (May and Wiedmeyer 1998) was considered. To avoid isobaric interference between $^{23}Na^{40}Ca^+$ and ^{63}Cu, as well as between $^{23}Na^{40}Ca^+$ and ^{63}Cu, processed solutions from sets 2 and 3 were purified by ion-exchange chromatography. The purified Cu solutions were performed through an anion exchange resin (Bio-rad® AG MP-1), applying the procedure described by Roebbert et al. (2018). The evaporated residue was dissolved in 1 ml 9 M HCl, and the purified Cu fractions were acquired by loading the solution with Bio-Rad®AG MP-1 anion resin in 2 ml Bio-Rad® columns. The cleaning of resin was carried out with 10 ml 7 M HCl, water, 5% HNO_3, and water before loading samples. The conditioning of resin was done by adding 12 ml 9 M HCl to the solutions. The samples were then loaded and the matrix was removed with 7 ml 9 M HCl. The Cu fractions were eluted with 18 ml 5 M HCl and dried. A mixture of concentrated HNO_3 and H_2O_2 solutions was added to the dryness. Based on the Cu concentration of solutions analyzed by ICP-OES, samples were further diluted to ~0.5 µg Cu /g in 3 % HNO_3 solution and doped with 1 µg/g Ni using a Ni NIST SRM 986 standard solution for Cu isotope measurement with solution nebulization MC-ICP-MS (Neptune, Thermo Scientific). More details about instrument setup and measurement procedure are provided by Lazarov and Horn (2015). Cu isotope compositions of the NIST C125-1 standard solution and the sample replicates were performed simultaneously to monitor the analytical precision and accuracy. Standard analyses are in agreement with the previously published values of Lazarov and Horn (2015). The overall uncertainty of isotopic composition measurements was generally better than 0.06‰ (2SD), with an average value of 0.03‰ (2SD). The daily reproducibility of the standard and samples was also better than 0.06‰ (2SD; Lazarov and Horn 2015).

The solid reactants and products mounted in resin were analyzed for their Cu isotope composition by in situ LA-MC-ICP-MS. An in-house built laser ablation system based on a UV-femtosecond-laser (Spectra-Physics) was combined with the aforementioned MC-ICP-MS. The laser system operates in the deep UV at 194 nm. Argon was used as the carrier gas. The NIST SRM 976 native Cu and two in-house chalcopyrite standards [cpy1 and cpy2; Lazarov and Horn (2015)] were measured as the known and unknown reference materials to verify whether the laser energy was set to the appropriate level and whether the obtained δ^{65}Cu values agreed with the values for the solution reported by Lazarov and Horn (2015). A spot diameter of 40 μm and laser repetition rates of 3−5 Hz and 10 Hz were used for NIST SRM 976 and cpy1-cpy2, respectively, which resulted in signal intensities of ~15 V on mass 65 (^{65}Cu). To maintain intensities similar to those observed for the standards, the cuprite pellets and secondary minerals were generally analyzed with a repetition rate of 5−7 and 10−30 Hz, respectively. Ablation of standards and samples was carried out by line mode to avoid potential depth effects, and the width of lines was ca. 28 μm. Thin layers of newly-formed minerals in Cp2 and 5 are generally wider than the ablation line (Fig.2a, d), however, newly-formed minerals in Cp4 have a width of 5-35 μm so there are only three data available for this sample (Fig.2c). There were at least 10 and 3 analyses available for cuprite and the overgrowth mineral, respectively.

For Cu isotope measurements of the solutions and solid phases, standard/sample bracketing and the Ni NIST SRM 986 standard solution were used to correct measured ^{65}Cu/^{63}Cu ratios for instrumental mass bias. The overall double relative standard error (2RSE, 2σ) for samples is less than 0.1‰, which is calculated by the propagation of within-run RSEs of a sample and its two bracketing standards.

4. RESULTS

4.1. Composition of solid phases

In Set 1, no discernible solid precipitates were observed after the reaction of Cu and Cu_2O with the HCl solution, respectively, at temperatures lower than ≤50°C. At moderate temperatures (300°C), native Cu, Cu-bearing minerals, and precipitates, as well as cuprite, were retrieved from the Cu_2O-HCl system (Fig. 2). It is worth noting that Cu_2O of Cp2 are both in the form of compacted powder (core) and mesh-like overgrowth layer (rim) adjacent to Cp2-S2 in Fig. 2b. Three types of solid products were obtained, namely, native Cu coating the Au capsule (S0), a solid mineral at the mantle of cuprite (S1; Fig. 2a), and precipitates separated from the quench fluid also covering the surface of the Cu_2O pellet (S2; Fig. 2b). The thickness of the overgrowth layer of S1 is about 200-400 μm (Fig.2a), and the replacement of Cp2 cuprite by S1 starts from the outer rim. Three to four spots were analyzed for S1 and S2 by EPMA. The data show that they have relatively low oxide totals (28.99−88.89 wt.%) and are mainly composed of Cu and Cl (Table 2). These low totals may originate from unmeasured H_2O, which has been confirmed by Raman spectroscopy. S2 analyses are qualitative since they show a thin coating on cuprite, and cuprite may be incorporated into their analyses. S2 is defined as hydrous Cu(II) in Table 2. The variability of S1 is mainly due to its varying degrees of hydration and has no relation to its thickness since the layer varies between 160 and 300 μm. Although atmospheric CO_2 can be purged into the starting solution, no peak of C-related species was found during the Raman analyses. Although Cu and Cu_2O were present in the capsule, the external oxygen fugacity was governed by the vessel, i.e., log $fO2$ of NNO+2.3 was lower than that required for Cu-Cu_2O. Thus, aqueous Cu(I) species predominate in the solution, and the potential formula of S1 could

345 be $CuCl \cdot nH_2O$ with the atomic ratios of Cu/Cl is ~1 (Table 2). Whereas the formula of S2 cannot
346 readily be revealed by EPMA data. Cuprite and precipitates were recovered at 800°C. A large
347 quantity of powder and white precipitates was collected from the quench fluid of the Cu_2O-HCl
348 system. The results of Qi et al. (2020) demonstrate that Cu_2O has been fully consumed and its
349 solubility in HCl was reached in DQ169. Furthermore, Qi et al. (2020) indicate that these
350 fine-grained precipitates are likely to be oversaturated CuCl crystals.

351 In Set 2, the initial Cu powder could not be retrieved, and the thin film of native Cu covered
352 the inner walls of the Au capsule at 600°C (Set 2). The color of these walls changed from deep
353 reddish to metallic given that the duration was prolonged from 0.17 to 96 h (Fig. 2h-l). Blue
354 precipitates deposited at the surface of the Au substrate were not analyzed due to their small
355 quantity (Fig.2h, j).

356 In Set 3, Cu-bearing minerals and cuprite were found, whereas Au bag coated by Cu was
357 not observed in 200°C, 20 MPa runs. A small number of white precipitates which consisted of Na,
358 Cu, and Cl (qualitative SEM analyses) were observed to cover the outer surface of Cp3 cuprite at
359 200°C, whereas thin layers of blue precipitates covered cuprite of Cp4, 5 (denoted as Cp4-S2 and
360 Cp5-S2 in Figs. 2c-d, respectively; Table 2). These solids precipitated at the outer rim of Cu_2O,
361 which show no crystalline form, and are most likely quench products produced from cooling.
362 Cp4-S is mainly composed of Cu (50−54 wt.%) with a composition similar to that of $CuO \cdot nH_2O$
363 reported in Qi (2019). Cp5-S consists of Cu and Cl with a Cu/Cl ratio of 1.6, the likely form is
364 hydrous copper chloride species. At 250°C, cuprite and native Cu covering the Au substrate were
365 recovered (Set 3). Other solids/precipitates could not be distinguished due to HCl/H_2O leaching
366 during post-treatment (described in Section 2). SEM analyses of solid precipitates on Au
367 capsules demonstrate that these phases are mainly composed of Cu, Cl, and Na.

368 **4.2. Cu content in fluid and isotope fractionation**

369 *4.2.1. Set 1 experiment*

370 In Cu-HCl systems, the Cu content in a 1 m HCl solution increases from 1026±51 to
371 1534±77 and 13159±658 μg g^{-1} at 25, 50, and 200°C (Table 3 and Fig. 3a), respectively.
372 Likewise, the Cu content of Cu_2O-HCl systems increases drastically from 5753±288 to
373 10727±536 μg g^{-1} at 25 and 50°C, respectively. It is worth mentioning that fluid inclusions in
374 DQ169 as a closed system give information about Cu_2O solubility in 1.5 m HCl at 800°C, i.e.,
375 64409±3220 μg g^{-1} Cu (Qi et al., 2020). The Cu content of quench fluids from this run is one
376 magnitude lower than the in situ fluid in this run due to the separation of solids.

377 Results from low-temperature (25−50°C) experiments show that Cu_2O dissolution in a 1 m
378 HCl solution is stronger by about 6 times than that of Cu dissolution in the Cu-HCl system (Fig.
379 3a). The extent of Cu isotope fractionation in the former one is much larger than the latter one,
380 i.e., $\Delta^{65}Cu_{fluid\text{-}Cu/Cu2O}$ values are up to 0.89±0.02‰ and 0.47±0.02‰, respectively (Fig. 3b). Both
381 Cu content and isotopic compositions in fluid indicate that acid leaching of Cu_2O is more
382 effective than metallic Cu. Moreover, the enhancement of Cu content in a fluid is attributed to
383 increasing temperature and chloride concentration. Fig. 3b shows that dissolved Cu yields
384 heavier isotope composition relative to their precursors except for two runs at 200 and 800°C
385 (DQ180 and DQ169). At 200°C the $\Delta^{65}Cu_{fluid\text{-}Cu}$ value of Cu-HCl system is -0.30±0.03‰,
386 whereas $\Delta^{65}Cu_{fluid\text{-}Cu}$ values turn to be 0.47±0.02‰ and -0.42±0.03‰ for Cu-HCl and
387 Cu-Cu_2O-HCl systems at 800°C, respectively (Fig.3b). These negative and positive
388 $\Delta^{65}Cu_{fluid\text{-}Cu/Cu2O}$ values are likely due to different mechanism (cf. Section 5.2).

389 At 300°C cuprite dissolution in HCl results in the formation of three types of secondary

solids, S0, S1, and S2 (see above). This run has the lowest Cu content of 538 μg g^{-1}, which is probably due to the removal of solid precipitates (S2) from fluids. Both S2 and the quench fluid yield positive δ^{65}Cu values above 1‰, and are 0.59−0.75‰ heavier than those of the precursor Cu_2O (Fig. 3b). Furthermore, the isotope composition of S2 is about 0.1‰ lower than that of the fluid, suggesting that S2 derived from the quench fluid. Both the neoformed mineral (S1) and native Cu (S0) yielded the same isotope signature of 0.23‰ (Table 3), and both values are much lower than that of Cu_2O, resulting in $\Delta^{65}Cu_{s1/S0\text{-}Cu2O}$ values of ca. -0.28‰ (Note that gray square and black circle are overlapped in Fig.3b). The $\Delta^{65}Cu_{s2\text{-}Cu2O}$ value is 0.75±0.03‰ (open square in Fig. 3b). These different Δ^{65}Cu values are likely due to their different oxidation states and chemical complexation.

4.2.2. Set 2 experiments

In the Cu-NaCl system, Cu content increases from 16±1 to 47±2 μg g^{-1} within 10 h and drops to 22±1 μg g^{-1} after 96 h (Fig. 4a). pH values of the experimental fluids are slightly acidic, i.e., varying between 5.52±0.48‰ and 5.72±0.39‰ (Table 1). In comparison, the Cu content of the Cu-HCl system is about three magnitudes higher than that of the Cu-NaCl system. Moreover, the quench fluid of the Cu-HCl system turned out to be more acidic than that of the Cu-NaCl system, namely, pH values of 0.3 and 5-6, respectively. Measured $\Delta^{65}Cu_{fl\text{-}Cu}$ values of the Cu-NaCl system increase from 0.42±0.02‰ to 0.63±0.02‰, 2.53±0.02‰ and 5.08±0.02‰ for experimental durations of 0.17, 1, 10, and 96 h, respectively (Fig. 4b). Moreover, the $\Delta^{65}Cu_{fl\text{-}Cu}$ value of the Cu-HCl system is 2.00±0.02‰, which is lower than that of Cu-NaCl system. On the other hand, observed Cu isotope fractionations between starting Cu and deposited Cu are 0.83±0.02‰ to 4.10±0.02‰ for the Cu-NaCl system at 0.17-96 h and 2.37±0.02‰ for Cu-HCl

412 at 21 h. The isotope compositions of deposited Cu are heavier than their precursor as well as the
413 associated fluids (Fig. 4b).

414 *4.2.3. Set 3 experiments*

415 In the Cu_2O–pH-buffered NaCl system (in situ and ex situ fluid-sampling runs), the Cu
416 content of the solution sampled in situ for the first time is mostly lower than that of the solution
417 sampled the second time in Cp3 at 200°C (Table 3). The inline sampled solution and the residual
418 solution in the Au cell are denoted as the in situ and quench fluids in Table 3, respectively. Cu
419 contents of the Cp3 in situ solutions are roughly twice those of Cp4 and Cp5 at 200°C (Fig. 5a),
420 which is likely due to the incorporation of Cu into precipitates for the latter two runs (Cp4-S2
421 and Cp5-S2) during the cooling process. Isotopically, the Cu isotope of all batches in Cp3 is
422 associated with their precursor following the mass balance rule at 200°C:

423 $$\delta^{65}Cu_{initial}=f_1\cdot\delta^{65}Cu_1+f_2\cdot\delta^{65}Cu_2 \quad (1)$$

424 Coefficients f_1 and f_2 are the mole fractions of the first and second sampled fluids, while $\delta^{65}Cu_1$
425 and $\delta^{65}Cu_2$ are their corresponding Cu isotope compositions. Similar to Eq. (1), the isotope
426 fractionation between the in situ fluid and Cu_2O of Cp3 is insignificant at 200°C, whereas
427 $\Delta^{65}Cu_{fl\text{-}Cu2O}$ value can reach 0.11±0.05‰ as temperature cools to 100°C (Fig. 5b).

428 Quench fluids of Cp4 and Cp5 yield much higher $\delta^{65}Cu$ values than Cu_2O, resulting in
429 $\Delta^{65}Cu_{fl\text{-}Cu2O}$ values of ~1‰ (Fig. 5b). Moreover, the $\Delta^{65}Cu_{S2\text{-}Cu2O}$ values of Cp4 and Cp5 are
430 negative (-0.72±0.03‰ and -0.25±0.32, respectively), implying that these solids were not
431 quenched precipitates from the fluid during cooling. For run Cp6, Cu contents of in situ fluids
432 increased by a factor of 4 with increasing temperature, i.e., from 832 to 3756 μg g^{-1} along a
433 heating course of 100−250°C within 6 h (Table 2, Fig. 5c). However, Cu content in fluid

decreased by ca. 1000 μg g^{-1} after 69 h, which was likely due to Cu partitioning between fluid and gas phases (cf. section 5.1). The $\Delta^{65}Cu_{\text{in situ fluid-Cu2O}}$ values show a coherent increase from -0.49±0.04‰ to 0.06±0.04‰ (except the first sampled fluid; Fig. 5d). The $\Delta^{65}Cu_{\text{quench fl.-Cu2O}}$ value is -0.29±0.04‰. In comparison, quench fluids of Cp7 and Cp8 yielded comparable isotope compositions as their precursors, i.e., $\Delta^{65}Cu_{\text{quench fluid-Cu2O}}$ value of ~0‰. Native Cu deposits of Cp6-8 have yielded rather constant $\delta^{65}Cu$ values of 0.35±0.02‰, resulting in $\Delta^{65}Cu_{\text{S0-Cu2O}}$ values of ca. -0.10±0.04‰.

5. DISCUSSION

5.1. Reaction mechanisms and Cu speciation

At 25−50°C, aqueous Cu(II) is likely the dominant species in the atmosphere with a $\log fO_2$ of -0.68, which is also confirmed by the Cu-O-H-Cl phase diagrams (Figs. 6a-b; Collings et al., 2000, Brugger et al., 2001). Reactions between Cu or Cu_2O and HCl solutions are presented by Qi et al., (2020) and as follows:

$$Cu_{(s)} + H^+_{(aq)} = Cu^+_{(aq)} + 1/2H_{2(g)} \quad (2)$$

$$Cu_2O_{(s)} + H^+_{(aq)} = 2Cu^+_{(aq)} + H_2O_{(aq)} \quad (3)$$

$$Cu^+_{(aq)} + H^+_{(aq)} = Cu^{2+}_{(aq)} + 1/2H_{2(g)} \quad (4)$$

where subscripts *aq* and *s* refer to the fluid phase and the solid phases, respectively. It can be seen from Figs. 6a-b that $CuCl^+$ may be the dominant species in solution at 25–50°C and 0.1 MPa. Thermodynamic calculations of Macdonald et al. (1972), Robie and Hemingway (1995), and Collings et al. (2000) show that $CuCl^+$ is a stable species in oxygenated and/or highly concentrated Cl-bearing solutions at 175°C. Moreover, spectroscopic observations of D'Angelo et al. (1997), Collings et al. (2000) and Brugger et al. (2001) demonstrate that Cu^{2+} and $CuCl^+$

456 are the dominant species in aqueous Cl-bearing solutions with minor amounts of $CuCl_2^0$ at 90°C.
457 To a lesser extent, aqueous Cu(I)Cl exists in fluids. A two-step reaction is involved during the
458 oxidation of Cu(0) to Cu(II), a fast and reversible transformation of native Cu to Cu(I), and a
459 slow and rate-determining process of Cu(I)-Cu(II) (Matisson and Bockris 1959).

460 Fulton et al. (2000b) as well as Brugger et al. (2001) demonstrate that Cu(I) is dominant in
461 solution at temperatures higher than 100°C and relatively reducing conditions ($\log fO_2$=NNO+2)
462 (Figs. 6c-d). Cuprite dissolution in HCl/NaCl solutions at temperatures higher than 200°C
463 follows the reaction (5). Cuprous complexes (primarily $CuCl_{(aq)}$, $CuCl_2^-$, $CuCl_3^{2-}$) predominate in
464 acidic solutions with low sulfur activity (e.g., Crerar and Barnes 1976; Xiao et al. 1998; Fulton et
465 al. 2000a; Mei et al. 2014) above 100°C. With increasing chloride concentration and temperature,
466 the proportion of $CuCl_3^{2-}$ becomes less dominant. Thermodynamic properties of Cu species are
467 extracted from the SUPCRT92 database (Johnson et al. 1992). Thermodynamic modeling of the
468 Cu-O-H-Cl phase diagram has been carried out by using the CHNOSZ software (Dick 2019). A
469 bi-acetate complex predominates at 250°C and 600°C (Figs. 6c-d), which is in accordance with
470 previous findings (e.g., Brugger et al., 2007; Liu et al., 2001).

471 Cuprite dissolves in HCl solutions mainly in the form of Cu^+ at 300°C (reaction 5). Both Cu
472 and Cu_2O were present after run Cp3. External oxygen fugacity governed by the vessel is $\log fO_2$
473 ~ NNO+2.3, which is lower than that required for buffering Cu and Cu_2O. Thus, in line with the
474 microscopic observation and EMP analyses of S1, cuprite has been replaced homogeneously in
475 Cp3 by a Cu(I)-bearing mineral, likely $CuCl \cdot nH_2O$. These mineral precipitates are likely formed
476 at the experimental stage and possibly due to CuCl oversaturation. Unlike Cp2-S1 the solids in
477 contact with Cu_2O in runs Cp4, 5 have various thicknesses and are much thinner than Cp2-S1.
478 Moreover, they have variable compositions including variable total oxides (30-60 wt.%) and

479 Cu/Cl ratios. This evidence might indicate that Cp4-S2 and Cp5-S2 precipitated from quench
480 fluid rather than formed at the experimental stage.

481 The formation of native Cu (S0) in Cu-HCl/NaCl systems at 250°C and 300°C is likely
482 produced via reaction (5), which is often observed in oxyacid solution (e.g., Wadsworth and
483 Wadia 1955).

484 $$2Cu^{+}_{(aq)} = Cu^{2+}_{(aq)} + Cu_{(s)} \quad (5)$$

485 Formation of metallic copper by reaction (5) is well known, e.g. the leaching of cuprite in an
486 oxyacidic solution such as sulfuric acid (Wadsworth and Wadia 1955; Park et al. 2017) or
487 perchloric acid (Majima et al. 1989). Moreover, Qi (2019) observed the replacement of cuprite
488 by Cu in both pure water and acetate-acetic-bearing solutions, which was ascribed to the Cu(I)
489 disproportionation reaction. Aqueous solutions contain both $Cu(I)_{aq}$ and $Cu(II)_{aq}$, and aqueous
490 Cu(I) species predominate in the solution (Equation 5). At 250°C the estimated content of Cu^{2+}
491 and Cu^{+} in solution may be 1000-1200 and 2000-2400 μg g^{-1}, respectively. Due to the
492 complexity of the system, solids such as Cu(II)-Ac may form and precipitate after the reaction
493 (5). Likewise, Qi (2019) observed tenorite (CuO) precipitates in Cu_2O-HAc-KAc systems at both
494 150 and 250°C, which was likely due to Cu(II) acetate decomposition. Moreover, acetate
495 decomposed into $CO_{2(g)}$ and $CH_{4(g)}$ after long time (~70 h) at 250°C (Qi, 2019).

496 At 600−800°C, native Cu reacts with HCl or NaCl solutions, which can be explained by
497 reactions (2) and (6), as suggested by Zajacz et al. (2011) and Qi et al. (2020):

498 $$2Cu_{(s)} + 2H_2O_{(aq)} + 2NaCl_{(aq)} \rightleftharpoons NaCuCl_{2(g)} + NaOH_{(aq)} + CuOH_{(aq)} + H_{2(g)} \quad (6)$$

499 Firstly, experimental conditions become more reducing than what is required to maintain the
500 stability of Cu-Cu_2O as the reaction evolves at 600-800°C, i.e., Cu^{+} is not stable. Secondly,
501 monovalent Cu(I)-bearing species would be reduced to Cu metal at the surface of Au/Cu

substrate, similar to Fig.3 presented in Qi et al. (2019). In addition, dissolved Cu is far less than the initial loading, i.e., products of 0.002–0.657 mg Cu relative to initial 11.12–12.21 mg in 600°C Cu±HCl/NaCl runs. Since no discernible solids are retained after these runs, Cu loss to the Au substrate could explain these large mass discrepancies. Next, based on the Cu-Au phase diagram Cu reacts with Au to form (Cu, Au) alloy at 600°C (Okamoto et al., 1987). Cu diffuses rapidly in both Cu and gold substrates at high temperatures (Kuper et al. 1954; Ravi and Paul 2012). Diffusional transport of Cu can be calculated based on the equation: $D = D_0 \exp(E_a/RT)$, where D_0 and E_a refer to the frequency factor ($m^2\ s^{-1}$) and activation energy ($kJ\ mol^{-1}$), respectively. The diffusion layer of Cu on both Cu and Au are 29 μm at 800°C (24 h; Kuper et al. 1954) and 1.92–45.54 μm at 600°C (0.17–96 h; Ravi and Paul 2012), respectively.

Solid precipitates (S2) separated from the quench fluid often appeared to be in powder form (e.g., DQ180) or scattered at the starting mineral surface (e.g., Cp3). This makes it difficult to discern whether they formed during experimental conditions or post-cooling processes.

5.2. Cu isotope fractionation mechanisms

The aforementioned reactions indicate that the observed fractionations are controlled by: (1) oxidation of Cu(0) to Cu(II) or Cu(I) to Cu(II) at 25−50°C; (2) disproportionation of Cu(I) to Cu(II) and Cu at 250−300°C, and (3) oxidation of Cu(0) to Cu(I) at 600−800°C.

At low temperatures (25−50°C), oxidative leaching/dissolution of native Cu in HCl solution induces less significant fractionation than that in the Cu_2O-HCl system. Isotope exchange between Cu(0) and Cu(II) is slower than Cu(I) to Cu(II) due to a two-step oxidation process, and hence the extent of isotope fractionation is smaller in the oxidation of Cu-Cu(II) than that of Cu(I)-Cu(II), e.g., Δ^{65}Cu values are 0.07−0.12‰ and 0.52−0.89‰ in the former and latter cases,

524 respectively. Fluids containing both Cu^{+} and Cu^{2+} may give rise to these positive values in
525 Cu/Cu_2O -HCl systems.

526 Dissolution of Cu_2O in pH-buffered NaCl/HCl solutions at both low (200°C, 48 h and
527 250°C, 6 h) and high (800°C) temperatures results in fluid enriched with light isotope (^{63}Cu),
528 about 0–0.55±0.04‰ lower than the precursor (Fig. 5b, d). When the temperature gets higher
529 than 250°C and the run duration extends to ~70 h, Cu(I) disproportionation reaction
530 predominates in fluids. A drop of 24% in Cu content after 69 h can be noticed from the
531 time/temperature resolved Cu content evolution curve (Fig.5c). On the one hand Cu(I)
532 disproportionation reaction will not cause any Cu variation (reaction 5), and another process (i.e.,
533 phase separation) is likely responsible for this drop. Acetate decomposition into $CO_{2(g)}$ and $CH_{4(g)}$
534 can occur at conditions similar to this study (Qi, 2019), and hence Cu partitions differently in the
535 coexisting gases and fluids. Vapor may sequester 200–490 μg g^{-1} Cu by considering dissolved Cu
536 of 2865 μg g^{-1} (69 h of Cp6 in Table 3) and $D_{Cu}^{V/L}$ of 0.07±0.1 ($D_{Cu}^{V/L}$ refers toV-L Cu
537 partitioning coefficient and is taken from Rempel et al., 2012). In addition, Archibald et al. (2002)
538 confirm that up to 280 μg g^{-1} Cu can be transferred by the vapor phase at 280–320°C. Phase
539 separation in these runs may overprint the redox process. In ex situ runs vapor phase will be lost
540 during capsule opening and evaporation so that the isotope composition of the final solution will
541 be different from that of the in situ run. Both in situ (Cp6) and ex situ runs (Cp7, 8) yield similar
542 $\delta^{65}Cu$ values of final solutions and similar $\Delta^{65}Cu_{Cu\text{-}Cu2O}$ values. This phase separation induces
543 insignificant isotope fractionation, and an experimental calibration provides evidence that $\delta^{65}Cu$
544 values of vapor and liquid were equal within uncertainty (Rempel et al., 2012). Redox process
545 results in the fluid mixed with Cu(I) and Cu(II) as well as enriched with heavy isotope, i.e.,
546 $\Delta^{65}Cu_{in\ situ\ fl\text{-}Cu2O}$ and $\Delta^{65}Cu_{quench\ fl\text{-}Cu2O}$ are up to 0.13±0.04‰ at 250°C and 0.59±0.03‰ at 300°C,

547 respectively. In contrast, the reduced Cu metal by reaction (5) has a relatively low δ^{65}Cu value,
548 e.g., $\Delta^{65}Cu_{Cu\text{-}Cu2O}$ of up to -0.28±0.03‰.

549 At high temperatures (600-800°C), both solid product (Cu) and fluid show a large
550 variability in δ^{65}Cu values, 0.79±0.02‰–5.45±0.02‰ (Table 3). This significant isotope
551 fractionation ($\Delta^{65}Cu_{quench\ fl/Cu\text{-}Cu}$) up to 5.08±0.02‰ cannot be simply explained by Cu(I)-Cu
552 oxidative dissolution, and hence, surface diffusion of Cu into Au/Cu during the annealing
553 process as well as the reduction from deposited Cu to Cu(I) in solution should be taken into
554 consideration to counterbalance the Cu isotopic budget. Mass transport of Cu-Cu(I) is unlikely to
555 induce significant isotope fractionation according to Qi et al., (2019). The diffusion of Cu
556 isotopes in same medium is mass dependent, and McLaughlin (1960) describes this as,

557 $$\frac{D_1}{D_2} = (\frac{M_2}{M_1})^{\gamma} \quad (10)$$

558 where D_1 and D_2 are the isotope-dependent diffusion coefficients of species with molecular mass
559 M_1 and M_2. The ratio of isotope diffusion coefficient ($D^{63}Cu/D^{65}Cu$) is 1.016 when diffusion
560 occurs in ideal gas and solution (γ=0.5; Jähne et al., 1987; McLaughlin, 1960). This indicates
561 that light isotope (^{63}Cu) transports faster than its heavy counterpart (^{65}Cu) in an ideal gas and
562 solution, which is also valid in other phases such as vapor, metal, sulfide, and melt (Savage et al.
563 2015; Huang et al. 2016b, 2017; Ni et al. 2021). Preferential enrichment of ^{65}Cu at the rim of the
564 surface diffusion layer is therefore attributed to the distinguished high δ^{65}Cu values of deposited
565 Cu (up to 4.47±0.02‰; Table 3). Nikitenkov et al. (2006) propose that diffusion transport can
566 cause a decreasing concentration of the prevalent isotope in a diffusion surface zone. Moreover,
567 they state that diffusion transport of Cu could cause significant isotope fractionation than that
568 indicated by Eq.(10). Further experiments are needed to confirm whether an isotopic
569 composition gradient exists along the diffusion profile. The final solutions yield similar δ^{65}Cu

values as the deposited Cu in these runs and have pH of ~5.7 and 0.3 for NaCl and HCl-bearing runs, respectively. Both pieces of evidence indicate that the neoformed Cu redissolves back to solutions via backward reactions (2, 6).

5.3. Post-quench effect on Cu isotope fractionation

The effects of different cooling rates on fractionation are investigated at 200-250°C with initial material, pressure, and run durations being equal, i.e., low cooling rate of 0.014 K s^{-1} (Cp3, 6) and high cooling rate of 25 K s^{-1} (Cp4-5, and Cp7-8) (Table 3). Both in situ and ex situ fluids were collected from Cp3, 6, whereas ex situ fluids were collected from Cp4-5 and Cp7-8. It is evident from Cp3 and Cp6 that cooling from 200°C to 100°C and from 250°C to 150°C results in an insignificant variation of isotope composition (less than 0.1‰, Fig.5). Moreover, the isotopic composition of 200°C in situ fluid agrees well with the quench solution of Cp3 at 25°C. The 250°C-solution sampled at 5.5 h agrees well with the quench solution of Cp6. At the same time, the sample solution after a long time (69 h) is 0.4‰ higher than that of the quench solution due to complex reactions. In contrast, different solid phases would form at an elevated cooling rate (25 K/s), e.g., hydrous Cu(II)-bearing minerals in Cp4 and Cp5, respectively. Moreover, quench fluids are ~0.9‰ higher than the initial cuprite whereas new solid phases are 0.25−0.72‰ lower than their initial solid phases, which are comparable to Cp6 runs. It is impossible to identify any solid deposits from Cp7 (duplication Cp8) since an improved method to process the dryness has been applied to them. It is interesting to note that δ^{65}Cu values of quench fluids of Cp7,8 are identical to that of in situ fluid of Cp6 at 69 h. Moreover, native Cu formed in all three runs yielded the same value. Three different solid phases (S0, S1, S2) were generated at 300°C in Cp2 with a cooling rate of 3 K/s. S0 and S1 have identical δ^{65}Cu values, implying that these phases

592 are formed from the same source. Both S0 and S1 are about 1‰ lower than S2, which have a
593 similar δ^{65}Cu value as its precursor fluid. The different isotope signatures in S0, S1, and S2 are
594 likely due to the rapid cooling process. Rapid quenching (3-25 K s^{-1}) results in different solids
595 formation, and hence induces significant isotope fractionation. The improved fluid treatment has
596 the advantage of avoiding the formation of post-quench solids.

597 **5.4. Implications**

598 The formation of native Cu in geological settings has been induced by reduction reactions,
599 with agents such as methane and organic compounds actively involved in these reactions (Dekov
600 et al., 2013; Markl et al., 2006). Alternatively, the results of this experimental study provide
601 further insight into the formation of native Cu in geological settings (e.g., seafloor and supergene
602 conditions), which may be formed due to Cu(I) disproportionation reactions, with product
603 aqueous Cu(II) species being lost or precipitated in the vicinity. This mechanism has not received
604 much attention in natural systems. Both this study and Qi et al. (2019) show that Cu(I)
605 disproportionation can occur in water, HCl, pH-buffered NaCl, and acetate solutions, which is
606 probably a function of temperature (e.g., 250−300°C in this study). Moreover, isotope
607 fractionation during native Cu dissolution and precipitation was determined, i.e., $\Delta^{65}Cu_{Cu\text{-}Cu(I)}$
608 values vary from -0.03±0.05‰ to -0.28±0.02‰ at 25 and 250−300°C, respectively. This enables
609 the use of Cu isotopes for tracing hydrothermal processes associated with the transformation of
610 Cu-bearing phases with different valence states (e.g., Dekov et al. 2013; Ikehata and Hirata 2012;
611 Eslami et al. 2021; Bornhorst and Mathur 2017).

612 Ore minerals crystallization (or recrystallization) is a key process for metal enrichment.
613 Using Cu isotopes as a proxy cannot only unravel their isotopic exchange through the

614 crystallization process but also trace the fluid pathway (Baggio et al., 2018; Chaudhari et al.,
615 2022; Syverson et al., 2021; Zeng et al., 2021). In oceanic crust and supergene settings, the
616 corresponding secondary Cu-bearing minerals often have different oxidation states including
617 native Cu, cuprite, and Cu(II) minerals (Larson et al., 2003; Markl et al., 2006). This study
618 shows that precipitation of neoformed Cu(I) minerals at 200 and 300°C can yield δ^{65}Cu of as low
619 as -0.26±0.02‰ and their complementary heavy ^{65}Cu is released into fluids, corresponding to
620 $\Delta^{65}Cu_{fluid\text{-}Cu2O}$ up to ~1‰ (Fig. 7). In the seafloor hydrothermal system, Rouxel et al. (2004)
621 reported that negative δ^{65}Cu values of massive sulfides may be interpreted by recrystallization,
622 supported by the experimental observation that Cu-bearing fluids are 0.22±0.32‰ heavier than
623 chalcopyrite during recrystallization (Syverson et al., 2021). Similarly, weathering processes
624 such as the supergene reworking of hypogene Cu(I) sulfides lead to isotopically heavier fluids
625 and lighter residual minerals (Mathur et al., 2010; Mirnejad et al., 2010). These data imply that
626 hydrothermal reworking can change the isotopic signature of Cu-bearing minerals even though
627 their oxidation state has not been modified. In cases in which minerals precipitate directly from
628 the fluid due to the cooling effect, it would induce a relatively insignificant Cu isotope
629 fractionation as demonstrated by our experimental data, i.e., Δ^{65}Cu values are less than 0.16±0.03‰
630 at temperatures of 200−800°C for those runs in which quench fluid precipitates are observed
631 (Table 3). Likewise, isotope fractionation up to 0.4‰ has been observed during the precipitation
632 of malachite or $Cu(OH)_2$ from Cu(II) solutions (Maréchal et al. 1999; Ehrlich et al. 2004).

633 The redox process exerts a strong effect on Cu isotope fractionation, and is shown in Fig. 7.
634 Previous experiments on the reduction of aqueous Cu(II) to Cu(I)-bearing sulfides or Cu(0)
635 induce fractionations varying from 1.21±0.06‰ to 4.03±0.13‰ at 2–200°C (Ehrlich et al., 2004;
636 Pękala et al., 2011; Qi et al., 2019; Zhu et al., 2002). Oxidative leaching of Cu(I) sulfides to

637 aqueous Cu(II) results in fractionations of 0.98±0.14–2.74±0.22‰ at atmospheric conditions
638 (Fernandez and Borrok, 2009; Kimball et al., 2009; Mathur et al., 2005). Similarly, oxidative
639 leaching of Cu/Cu_2O by HCl or NaCl solutions can induce fractionation of up to 1‰ at 25-300°C
640 and up to 5.08±0.02‰ at 600-800°C in this study. Furthermore, the $\Delta^{65}Cu$ values in this study
641 during Cu_2O oxidative leaching at 200-300°C are in good agreement with the prediction
642 extrapolation of Qi et al. (2019) and Ehrlich et al. (2004) (Fig. 7). This also indicates that metal
643 complexing ligands of S^{2-} and Cl^- may have similar effects on Cu isotope fractionation. The most
644 significant isotope fractionation of 4.03±0.13‰ has been observed during the reduction of Cu^{2+}
645 to CuI (Zhu et al., 2002). This is likely due to the largest ionic radius of I relative to Cl and S. In
646 comparison to I, S and Cl form stiffer bonds with Cu and concentrate heavy isotope of ^{65}Cu
647 (Schauble, 2004). Evidence show that the transformation of Cu-Cu(I) at low temperature (≤
648 300°C) does not induce significant isotope fractionation, e.g., -0.08±0.05‰ of this study, and
649 almost 0‰ in natural (Markl et al., 2006), experimental (Qi et l., 2019) samples and theoretical
650 prediction (Fig. 7; Liu et al., 2021; Sherman 2013).

651 Phase separation, specifically vapor-liquid (V-L) separation related to fluid boiling, is a key
652 process for metal enrichment in ore systems. V-L separation can decrease Cu content by 24% in
653 this study. Both this study and Rempel et al. (2012) demonstrate that V-L fractionation of Cu
654 isotopes would be conservative in a closed system. In contrast, V-L separation can cause
655 significant Cu isotope fractionation in natural open systems. For example, Yao et al. (2016)
656 investigated Cu and Mo isotopes of the cogenetic chalcopyrite and molybdenite of the Dahutang
657 W-Cu-Mo ore in China. They observed a negative correlation between $\delta^{65}Cu$ (-0.31‰–1.48‰)
658 and $\delta^{97}Mo$ (-0.03‰–1.06‰). They attribute this negative trend to V-L separation, which causes
659 Cu and Mo isotopes to partition differently in the coexisting phases. Zegkinoglou et al. (2023)

660 analyzed the Cu isotope composition of primary pyrite and orpiment from seafloor massive
661 sulfide diffuser vents in the Hellenic volcanic arc. Two types of pyrite have been found, and their
662 δ^{65}Cu values are -0.94‰– 0.25‰ and -0.45‰– -0.09‰ for pyrite-I, and II, respectively. To date,
663 orpiment shows the most extreme variability in δ^{65}Cu values, i.e., 1.90‰ – 25.73‰. They
664 propose that continuous boiling and Rayleigh distillation can contribute to the large range of
665 δ^{65}Cu, and sulfides that crystallize from the ^{65}Cu-enriched vapor can yield substantially high
666 δ^{65}Cu (e.g., 25.73‰). Zhao et al. (2023) apply multiple isotopes (H-O-S-Cu) to investigate the
667 mineralization event in a Chinese shear-zone-hosted Cu deposit. They observe two episodes of
668 sulfide, and their δ^{65}Cu values are -1.85‰ – 0.39‰ and -0.030‰ – -0.05‰ for the early and late
669 stages, respectively. The progressive increasing δ^{65}Cu values can be explained by the vapor
670 transport of ^{63}Cu.

671 **Declaration of Competing Interest**

672 The authors declare that they have no known competing financial interests or personal
673 relationships that could have appeared to influence the work reported in this paper.

674 **Acknowledgments**

675 This research was supported by the National Natural Science Foundation of China (42002059,
676 41972055), the Natural Science Foundation of Xinjiang Uygur Autonomous Region, China
677 (2020D01C074), Open Project of Key Laboratory, Xinjiang Uygur Autonomous Region, China
678 (2023D04067), the Key Research and Development Program of Xinjiang Uygur Autonomous
679 Region, China (2022B03015-2) and the German Academic Exchange Service
680 (DAAD-57076462).

References

Asael, D., Matthews, A., Bar-Matthews, M., and Halicz, L. (2007) Copper isotope fractionation in sedimentary copper mineralization (Timna Valley, Israel). Chemical Geology, 243, 238–254.

Asael, D., Matthews, A., Bar-Matthews, M., Harlavan, Y., and Segal, I. (2012) Tracking redox controls and sources of sedimentary mineralization using copper and lead isotopes. Chemical Geology, 310–311, 23–35.

Asael, D., Matthews, A., Oszczepalski, S., Bar-Matthews, M., and Halicz, L. (2009) Fluid speciation controls of low temperature copper isotope fractionation applied to the Kupferschiefer and Timna ore deposits. Chemical Geology, 262, 147–158.

Berkenbosch, H.A., de Ronde, C.E.J., Paul, B.T., and Gemmell, J.B. (2015) Characteristics of Cu isotopes from chalcopyrite-rich black smoker chimneys at Brothers volcano, Kermadec arc, and Niuatahi volcano, Lau basin. Mineralium Deposita, 50, 811–824.

Berndt, J., Holtz, F., and Koepke, J. (2001) Experimental constraints on storage conditions in the chemically zoned phonolitic magma chamber of the Laacher See volcano. Contributions to Mineralogy and Petrology.

Berry, A.J., Hack, A.C., Mavrogenes, J.A., Newville, M., and Sutton, S.R. (2006) AXANES study of Cu speciation in high-temperature brines using synthetic fluid inclusions. American Mineralogist, 91, 1773–1782.

Bornhorst, T.J., and Mathur, R. (2017) Copper isotope constraints on the genesis of the keweenaw peninsula native copper district, Michigan, USA. Minerals, 7.

Brugger, J., McPhail, D.C., Black, J., and Spiccia, L. (2001) Complexation of metal ions in brines: Application of electronic spectroscopy in the study of the Cu(II)-LiCl-H2O

systembetween 25 and 90°C. Geochimica et Cosmochimica Acta, 65, 2691–2708.

Brzozowski, M.J., Good, D.J., Wu, C., and Li, W. (2021) Cu isotope systematics of conduit-type Cu–PGE mineralization in the Eastern Gabbro, Coldwell Complex, Canada. Mineralium Deposita, 56, 707–724.

Busigny, V., Chen, J. Bin, Philippot, P., Borensztajn, S., and Moynier, F. (2018) Insight into hydrothermal and subduction processes from copper and nitrogen isotopes in oceanic metagabbros. Earth and Planetary Science Letters, 498, 54–64.

Butrymowicz, D.B., Manning, J.R., and Read, M.E. (1974) Diffusion in Copper and Copper Alloys, Part II. Copper Silver and Copper Gold Systems. Journal of Physical and Chemical Reference Data, 3, 527–602.

Collings, M.D., Sherman, D.M., and Ragnarsdottir, K.V. (2000) Complexation of Cu2+ in oxidized NaCl brines from 25°C to 175°C: Results from in situ EXAFS spectroscopy. Chemical Geology, 167, 65–73.

Crerar, D.A., and Barnes, H.L. (1976) Ore Solution Chemistry V. Solubilities of Chalcopyrite and Chalcocite Assemblages in Hydrothermal Solution at 200° to 350°C, 71, 772–794.

D'Angelo, P., Bottari, E., Festa, M.R., Nolting, H.F., and Pavel, N. V. (1997) Structural investigation of copper(II) chloride solutions using x-ray absorption spectroscopy. Journal of Chemical Physics, 107, 2807–2812.

Dekov, V.M., Rouxel, O., Asael, D., Hålenius, U., and Munnik, F. (2013) Native Cu from the oceanic crust: Isotopic insights into native metal origin. Chemical Geology, 359, 136–149.

Derrey, I.T., Albrecht, M., Dupliy, E., Botcharnikov, R.E., Horn, I., Junge, M., Weyer, S., and Holtz, F. (2017) Experimental tests on achieving equilibrium in synthetic fluid inclusions: Results for scheelite, molybdenite, and gold solubility at 800°C and 200 MPa. American

727 Mineralogist, 102, 275–283.
728 Dick, J.M. (2019) CHNOSZ: Thermodynamic calculations and diagrams for geochemistry.
729 Frontiers in Earth Science, 7, 1–18.
730 Dickson, F.W., Blount, C.., and Tunell, G. (1963) Use of hydrothermal solution equipment to
731 determine the solubility of anhydrite in water from 100°C to 275°C and from 1 bar to 1000
732 bars.pdf.
733 Duan, J., Tang, J., Li, Y., Liu, S.-A., Wang, Q., Yang, C., and Wang, Y. (2016) Copper isotopic
734 signature of the Tiegelongnan high-sulfidation copper deposit, Tibet: implications for its
735 origin and mineral exploration. Mineralium Deposita, 51, 591–602.
736 Ehrlich, S., Butler, I., Halicz, L., Rickard, D., Oldroyd, A., and Matthews, A. (2004)
737 Experimental study of the copper isotope fractionation between aqueous Cu(II) and
738 covellite, CuS. Chemical Geology, 209, 259–269.
739 Eslami, A., Malvoisin, B., Grieco, G., Aradi, L.E., Marchesi, C., Cavallo, A., Montanini, A.,
740 Borghini, G., Mathur, R., Ikehata, K., and others (2021) Native copper formation associated
741 with serpentinization in the Cheshmeh-Bid ophiolite massif (Southern Iran). Lithos, 382–
742 383.
743 Fernandez, A., and Borrok, D.M. (2009) Fractionation of Cu, Fe, and Zn isotopes during the
744 oxidative weathering of sulfide-rich rocks. Chemical Geology, 264, 1–12.
745 Fujii, T., Moynier, F., Abe, M., Nemoto, K., and Albarède, F. (2013) Copper isotope fractionation
746 between aqueous compounds relevant to low temperature geochemistry and biology.
747 Geochimica et Cosmochimica Acta, 110, 29–44.
748 Fujii, T., Moynier, F., Blichert-Toft, J., and Albarède, F. (2014) Density functional theory
749 estimation of isotope fractionation of Fe, Ni, Cu, and Zn among species relevant to

geochemical and biological environments. Geochimica et Cosmochimica Acta, 140, 553–576.

Fulton, J.L., Hoffmann, M.M., and Darab, J.G. (2000a) An X-ray absorption fine structure study of copper(I) chloride coordination structure in water up to 325°C. Chemical Physics Letters, 330, 300–308.

Fulton, J.L., Hoffmann, M.M., Darab, J.G., Palmer, B.J., and Stern, E.A. (2000b) Copper(I) and Copper(II) Coordination Structure under Hydrothermal Conditions at 325°C: An X-ray Absorption Fine Structure and Molecular Dynamics Study. Journal of Physical Chemistry A, 104, 11651–11653.

Gregory, M.J., and Mathur, R. (2017) Understanding Copper Isotope Behavior in the High Temperature Magmatic-Hydrothermal Porphyry Environment. Geochemistry, Geophysics, Geosystems, 18, 4000–4015.

Guo, H., Xia, Y., Bai, R., Zhang, X., and Huang, F. (2020) Experiments on Cu-isotope fractionation between chlorine-bearing fluid and silicate magma: Implications for fluid exsolution and porphyry Cu deposits. National Science Review, 7, 1319–1330.

Hack, A.C., and Mavrogenes, J.A. (2006) A cold-sealing capsule design for synthesis of fluid inclusions and other hydrothermal experiments in a piston-cylinder apparatus. American Mineralogist, 91, 203–210.

Hannington, M.D., Thompson, G., Rona, P.A., and Scott, S.D. (1988) Gold and native copper in supergene sulphides from the Mid-Atlantic Ridge. Nature 1988 333:6168, 333, 64–66.

Huang, J., Liu, S.A., Gao, Y., Xiao, Y., and Chen, S. (2016a) Copper and zinc isotope systematics of altered oceanic crust at IODP Site 1256 in the eastern equatorial Pacific. Journal of Geophysical Research: Solid Earth, 3782–3803.

773 Huang, J., Liu, S.-A., Wörner, G., Yu, H., and Xiao, Y. (2016b) Copper isotope behavior during
774 extreme magma differentiation and degassing: a case study on Laacher See phonolite tephra
775 (East Eifel, Germany). Contributions to Mineralogy and Petrology, 171, 1–16.

776 Huang, J., Huang, F., Wang, Z., Zhang, X., and Yu, H. (2017) Copper isotope fractionation
777 during partial melting and melt percolation in the upper mantle: Evidence from massif
778 peridotites in Ivrea-Verbano Zone, Italian Alps. Geochimica et Cosmochimica Acta, 211,
779 48–63.

780 Huebner, J.S., and Sato, M. (1970) The oxygen fugacity-temperature relationships of manganese
781 oxide and nickel oxide buffers. American Mineralogist: Journal of Earth and Planetary
782 Materials, 55, 934–952

783 Ijichi, Y., Ohno, T., and Sakata, S. (2018) Copper isotopic fractionation during adsorption on
784 manganese oxide: Effects of pH and desorption. Geochemical Journal, 52, e1–e6.

785 Ikehata, K., and Hirata, T. (2012) Copper isotope characteristics of copper-rich minerals from the
786 horoman peridotite complex, Hokkaido, Northern Japan. Economic Geology, 107, 1489–
787 1497.

788 Ikehata, K., Notsu, K., and Hirata, T. (2011) Copper isotope characteristics of copper-rich
789 minerals from besshi-type volcanogenic massive sulfide deposits, Japan, determined using a
790 femtosecond LA-MC-ICP-MS. Economic Geology, 106, 307–316.

791 Johnson, J.W., Oelkers, E.H., and Helgeson, H.C. (1992) SUPCRT92: A software package for
792 calculating the standard molal thermodynamic properties of minerals, gases, aqueous
793 species, and reactions from 1 to 5000 bar and 0 to 1000°C, 899–947 p. Computers and
794 Geosciences Vol. 18.

795 Kharaka, Y.K., Carothers, W.W., and Rosenbauer, R.J. (1983) Thermal decarboxylation of acetic

796 acid: implications for origin of natural gas. Geochimica et Cosmochimica Acta, 47, 397–
797 402.
798 Kidder, J.A., Voinot, A., Leybourne, M.I., Layton-Matthews, D., and Bowell, R.J. (2021) Using
799 stable isotopes of Cu, Mo, S, and 87Sr/86Sr in hydrogeochemical mineral exploration as
800 tracers of porphyry and exotic copper deposits. Applied Geochemistry, 128.
801 Kim, Y., Lee, I., Oyungerel, S., Jargal, L., and Tsedenbal, T. (2019) Cu and S isotopic signatures
802 of the Erdenetiin Ovoo porphyry Cu-Mo deposit, northern Mongolia: Implications for their
803 origin and mineral exploration. Ore Geology Reviews, 104, 656–669.
804 Kuper, A., Letaw Jr, H., Slifkin, L., Sonder, E., and Tomizuka, C. (1954) Self-diffusion in copper.
805 Physical Review, 96, 1224.
806 Kimball, B.E., Mathur, R., Dohnalkova, A.C., Wall, A.J., Runkel, R.L., and Brantley, S.L. (2009)
807 Copper isotope fractionation in acid mine drainage. Geochimica et Cosmochimica Acta, 73,
808 1247–1263.
809 Larson, P.B., Maher, K., Ramos, F.C., Chang, Z., Gaspar, M., and Meinert, L.D. (2003) Copper
810 isotope ratios in magmatic and hydrothermal ore-forming environments. Chemical Geology,
811 201, 337–350.
812 Lazarov, M., and Horn, I. (2015) Matrix and energy effects during in-situ determination of Cu
813 isotope ratios by ultraviolet-femtosecond laser ablation multicollector inductively coupled
814 plasma mass spectrometry. Spectrochimica Acta - Part B Atomic Spectroscopy, 111, 64–73.
815 Li, W., Jackson, S.E., Pearson, N.J., and Graham, S. (2010) Copper isotopic zonation in the
816 Northparkes porphyry Cu-Au deposit, SE Australia. Geochimica et Cosmochimica Acta, 74,
817 4078–4096.
818 Lide, R.D. (1997) Handbook of chemistry and physics. New York: CRC.-90th Edition.-2010.

819 Liu, S., Li, Y., Liu, Jie, Yang, Z., Liu, Jianming, and Shi, Y. (2021) Equilibrium Cu isotope
820 fractionation in copper minerals: a first-principles study. Chemical Geology, 564, 120060.
821 Liu, S.A., Liu, P.P., Lv, Y., Wang, Z.Z., and Dai, J.G. (2019) Cu and Zn isotope fractionation
822 during oceanic alteration: Implications for Oceanic Cu and Zn cycles. Geochimica et
823 Cosmochimica Acta, 257, 191–205.
824 Liu, W., McPhail, D.C., and Brugger, J. (2001) An experimental study of copper(I)-chloride and
825 copper(I)-acetate complexing in hydrothermal solutions between 50°C and 250°C and
826 vapor-saturated pressure. Geochimica et Cosmochimica Acta, 65, 2937–2948.
827 Luczaj, J., and Huang, H. (2018) Copper and sulfur isotope ratios in Paleozoic-hosted
828 Mississippi Valley-type mineralization in Wisconsin, USA. Applied Geochemistry, 89, 173–
829 179.
830 Macdonald, D., Shierman, G., and Butler, P. (1972) Thermodynamics of metal--water systems at
831 elevated temperatures. Part 1. The water and copper--water systems.
832 Maher, K.C., and Larson, P.B. (2007) Variation in Copper Isotope Ratios and Controls on
833 Fractionation in Hypogene Skarn Mineralization at Coroccohuayco and Tintaya, Perú
834 Economic Geology, 102, 225–237.
835 Maher, K.C., Jackson, S., and Mountain, B. (2011) Experimental evaluation of the fluid-mineral
836 fractionation of Cu isotopes at 250deg;C and 300°C. Chemical Geology, 286, 229–239.
837 Majima, H., Awakura, Y., Enami, K., Ueshima, H., and Hirato, T. (1989) Kinetic study of the
838 dissolution of cuprite in oxyacid solutions. Metallurgical Transactions B, 20, 573–580.
839 Maréchal, C.N., Télouk, P., and Albarède, F. (1999) Precise analysis of copper and zinc isotopic
840 compositions by plasma-source mass spectrometry. Chemical Geology, 156, 251–273.
841 Markl, G., Lahaye, Y., and Schwinn, G. (2006) Copper isotopes as monitors of redox processes

842 in hydrothermal mineralization. Geochimica et Cosmochimica Acta, 70, 4215–4228.
843 Mason, T.F.D., Weiss, D.J., Chapman, J.B., Wilkinson, J.J., Tessalina, S.G., Spiro, B., Horstwood,
844 M.S.A., Spratt, J., and Coles, B.J. (2005) Zn and Cu isotopic variability in the Alexandrinka
845 volcanic-hosted massive sulphide (VHMS) ore deposit, Urals, Russia. Chemical Geology,
846 221, 170–187.
847 Mathur, R., Dendas, M., Titley, S., and Phillips, A. (2010) Patterns in the copper isotope
848 composition of minerals in porphyry copper deposits in Southwestern United States.
849 Economic Geology, 105, 1457–1467.
850 Mathur, R., Ruiz, J., Titley, S., Liermann, L., Buss, H., and Brantley, S. (2005) Cu isotopic
851 fractionation in the supergene environment with and without bacteria. Geochimica et
852 Cosmochimica Acta, 69, 5233–5246.
853 Mathur, R., Titley, S., Barra, F., Brantley, S., Wilson, M., Phillips, A., Munizaga, F., Maksaev, V.,
854 Vervoort, J., and Hart, G. (2009) Exploration potential of Cu isotope fractionation in
855 porphyry copper deposits. Journal of Geochemical Exploration, 102, 1–6.
856 Matisson, E., and Bockris, J.O.M. (1959) Galvanostatic studies of the kinetics of deposition and
857 dissolution in the copper + copper sulphate system. Transactions of the Faraday Society, 55,
858 1586–1601.
859 May, T.W., and Wiedmeyer, R.H. (1998) A Table of Polyatomic Interferences in ICP-MS Isotope
860 Abundance Interference. Atomic Spectroscopy, 19, 150–155.
861 McLaughlin, E. (1960) Transport coefficient ratios for isotopically substituted molecules in the
862 liquid phase and the transport mechanism. Physica, 26, 650–652.
863 Mei, Y., Liu, W., Sherman, D.M., and Brugger, J. (2014) Metal complexation and ion hydration
864 in low density hydrothermal fluids: Ab initio molecular dynamics simulation of Cu(I) and

Au(I) in chloride solutions (25-1000°C, 1-5000bar). Geochimica et Cosmochimica Acta, 131, 196–212.

Mirnejad, H., Mathur, R., Einali, M., Dendas, M., Alirezaei, S., 2010. A comparative copper isotope study of porphyry copper deposits in Iran. Geochem. Explor. Environ. Anal. 10, 413–418. https://doi.org/10.1144/1467-7873/09-229

Molnár, F., Mänttäri, I., O'Brien, H., Lahaye, Y., Pakkanen, L., Johanson, B., Käpyaho, A., Sorjonen-Ward, P., Whitehouse, M., and Sakellaris, G. (2016) Boron, sulphur and copper isotope systematics in the orogenic gold deposits of the Archaean Hattu schist belt, eastern Finland. Ore Geology Reviews, 77, 133–162.

Mountain, B.W., and Seward, T.M. (1999) The hydrosulphide/sulphide complexes of copper(I): Experimental determination of stoichiometry and stability at 22°C and reassessment of high temperature data. Geochimica et Cosmochimica Acta, 63, 11–29.

Mountain, B.W., and Seward, T.M. (2003) Hydrosulfide/sulfide complexes of copper(I): Experimental confirmation of the stoichiometry and stability of Cu(HS)2- to elevated temperatures. Geochimica et Cosmochimica Acta, 67, 3005–3014.

Ni, P., Macris, C.A., Darling, E.A., and Shahar, A. (2021) Evaporation-induced copper isotope fractionation: Insights from laser levitation experiments. Geochimica et Cosmochimica Acta, 298, 131–148.

Nikitenkov, N.N., Kolokolov, D.Yu., Chernov, I.P., and Tyurin, Yu.I. (2006) SIMS investigations of isotope effects at a processed solid surface. Vacuum, 81, 202–210.

Okamoto, H., Chakrabarti, D., Laughlin, D., and Massalski, T. (1987) The Au- Cu (gold-copper) system. Journal of Phase Equilibria, 8, 454–474.

Palmer, D.A., and Drummond, S.E. (1986) Thermal decarboxylation of acetate. Part I. The

kinetics and mechanism of reaction in aqueous solution. Geochimica et Cosmochimica Acta, 50, 813–823.

Park, I., Yoo, K., Alorro, R.D., Kim, M., and Kim, S. (2017) Leaching of copper from cuprous oxide in aerated sulfuric acid. Materials Transactions, 58, 1500–1504.

Pękala, M., Asael, D., Butler, I.B., Matthews, A., and Rickard, D. (2011) Experimental study of Cu isotope fractionation during the reaction of aqueous Cu(II) with Fe(II) sulphides at temperatures between 40 and 200°C. Chemical Geology, 289, 31–38.

Pouchou, J.-L., and Pichoir, F. (1991) Quantitative Analysis of Homogeneous or Stratified Microvolumes Applying the Model "PAP." In Electron Probe Quantitation pp. 31–75. Springer US.

Qi, D., Behrens, H., Botcharnikov, R., Derrey, I., Holtz, F., Zhang, C., Li, X., and Horn, I. (2020) Reaction between Cu-bearing minerals and hydrothermal fluids at 800°C and 200 MPa: Constraints from synthetic fluid inclusions. American Mineralogist, 105, 1126–1139.

Qi, D., Behrens, H., Lazarov, M., and Weyer, S. (2019) Cu isotope fractionation during reduction processes in aqueous systems: evidences from electrochemical deposition. Contributions to Mineralogy and Petrology, 174.

Qi, D. (2019) Isotopic and elemental distribution of copper between Cu-bearing minerals and aqueous fluids: implications of an experimental study. PhD Thesis, Leibniz University of Hannover.

Ravi, R., and Paul, A. (2012) Diffusion mechanism in the gold-copper system. Journal of Materials Science: Materials in Electronics, 23, 2152–2156.

Rempel, K.U., Liebscher, A., Meixner, A., Romer, R.L., and Heinrich, W. (2012) An experimental study of the elemental and isotopic fractionation of copper between aqueous

911 vapour and liquid to 450°C and 400bar in the CuCl-NaCl-H 2O and CuCl-NaHS-NaCl-H
912 2O systems. Geochimica et Cosmochimica Acta, 94, 199–216.
913 Ripley, E.M., Dong, S., Li, C., and Wasylenki, L.E. (2015) Cu isotope variations between
914 conduit and sheet-style Ni-Cu-PGE sulfide mineralization in the Midcontinent Rift System,
915 North America. Chemical Geology, 414, 59–68.
916 Robie, R.A., and Hemingway, B.S. (1995) Thermodynamic properties of minerals and related
917 substances at 298.15 K and 1 bar (10^5 pascals) pressure and at higher temperatures, 461 p.
918 Roebbert, Y., Rabe, K., Lazarov, M., Schuth, S., Schippers, A., Dold, B., and Weyer, S. (2018)
919 Fractionation of Fe and Cu isotopes in acid mine tailings: Modification and application of a
920 sequential extraction method. Chemical Geology, 493, 67–79.
921 Roedder, E. (1984) Fluid Inclusions. Reviews in mineralogy.
922 Rouxel, O., Fouquet, Y., and Ludden, J.N. (2004) Copper isotope systematics of the Lucky Strike,
923 Rainbow, and Logatchev sea-floor hydrothermal fields on the Mid-Atlantic Ridge.
924 Economic Geology, 99, 585–600.
925 Savage, P.S., Moynier, F., Chen, H., Shofner, G., Siebert, J., Badro, J., and Puchtel, I.S. (2015)
926 Copper isotope evidence for large-scale sulphide fractionation during Earth's differentiation.
927 Geochemical Perspectives Letters, 53–64.
928 Schauble, E.A. (2004) Applying stable isotope fractionation theory to new systems. Reviews in
929 mineralogy and geochemistry, 55, 65–111.
930 Schmidt, C., Watenphul, A., Jahn, S., Schäpan, I., Scholten, L., Newville, M.G., and Lanzirotti,
931 A. (2018) Copper complexation and solubility in high-temperature hydrothermal fluids: A
932 combined study by Raman, X-ray fluorescence, and X-ray absorption spectroscopies and ab
933 initio molecular dynamics simulations. Chemical Geology, 494, 69–79.

Seo, J.H., Lee, S.K., and Lee, I. (2007) Quantum chemical calculations of equilibrium copper (I) isotope fractionations in ore-forming fluids. Chemical Geology, 243, 225–237.

Seyfried, W.E., Gordon, P.C., and Dickson, F.W. (1979) A new reaction cell for hydrothermal solution equipment. American Mineralogist, 64, 646–649.

Sherman, D.M. (2013) Equilibrium isotopic fractionation of copper during oxidation/reduction, aqueous complexation and ore-forming processes: Predictions from hybrid density functional theory. Geochimica et Cosmochimica Acta, 118, 85–97.

Sherman, D.M., and Little, S.H. (2020) Isotopic disequilibrium of Cu in marine ferromanganese crusts: Evidence from ab initio predictions of Cu isotope fractionation on sorption to birnessite. Earth and Planetary Science Letters, 549.

Syverson, D.D., Borrok, D.M., Niebuhr, S., and Seyfried, W.E. (2021) Chalcopyrite-dissolved Cu isotope exchange at hydrothermal conditions: Experimental constraints at 350 °C and 50 MPa. Geochimica et Cosmochimica Acta, 298, 191–206.

Tompkins, H.G., and Pinnel, M.R. (1976) Low-temperature diffusion of copper through gold. Journal of Applied Physics, 47, 3804–3812.

Ulrich, T., Günther, D., and Heinrich, C.A. (1999) Gold concentrations of magmatic brines and the metal budget of porphyry copper deposits. Nature, 399, 676–679.

Wadsworth, M.E., and Wadia, D.R. (1955) Reaction rate study of the dissolution of cuprite in sulphuric acid. Jom, 7, 755–759.

Wang, C., Bagas, L., Chen, J., Yang, L., Zhang, D., Du, B., and Shi, K. (2018) The genesis of the Liancheng Cu–Mo deposit in the Lanping Basin of SW China: Constraints from geology, fluid inclusions, and Cu–S–H–O isotopes. Ore Geology Reviews, 92, 113–128.

Wang, P., Dong, G., Santosh, M., Liu, K., and Li, X. (2017) Copper isotopes trace the evolution

957 of skarn ores: A case study from the Hongshan-Hongniu Cu deposit, southwest China. Ore
958 Geology Reviews, 88, 822–831.
959 Wu, L., Hu, R., Li, X., Liu, S., Tang, YanWen, and Tang, YongYong (2017) Copper isotopic
960 compositions of the Zijinshan high-sulfidation epithermal Cu–Au deposit, South China:
961 Implications for deposit origin. Ore Geology Reviews, 83, 191–199.
962 Xiao, Z., Gammons, C.H., and Williams-Jones, A.E. (1998) Experimental study of copper(I)
963 chloride complexing in hydrothermal solutions at 40 to 300°C and saturated water vapor
964 pressure. Geochimica et Cosmochimica Acta, 62, 2949–2964.
965 Yao, J., Mathur, R., Sun, W., Song, W., Chen, H., Mutti, L., Xiang, X., and Luo, X. (2016)
966 Fractionation of Cu and Mo isotopes caused by vapor-liquid partitioning, evidence from the
967 Dahutang W-Cu-Mo ore field. Geochemistry Geophysics Geosystems, 17, 1312–1338.
968 Zajacz, Z., Seo, J.H., Candela, P.A., Piccoli, P.M., and Tossell, J.A. (2011) The solubility of
969 copper in high-temperature magmatic vapors: A quest for the significance of various
970 chloride and sulfide complexes. Geochimica et Cosmochimica Acta, 75, 2811–2827.
971 Zeng, Z., Li, X., Chen, S., de Jong, J., Mattielli, N., Qi, H., Pearce, C., and Murton, B.J. (2021)
972 Iron, copper, and zinc isotopic fractionation in seafloor basalts and hydrothermal sulfides.
973 Marine Geology, 436, 106491.
974 Zegkinoglou, N.N., Mathur, R., Kilias, S.P., Godfrey, L., Pletsas, V., Nomikou, P., and
975 Zaronikola, N. (2023) Boiling-induced extreme Cu isotope fractionation in sulfide minerals
976 forming by active hydrothermal diffusers at the Aegean Kolumbo volcano: Evidence from
977 in situ isotope analysis. Geology.
978 Zhang, Z., Mao, J., Wang, F., and Pirajno, F. (2006) Native gold and native copper grains
979 enclosed by olivine phenocrysts in a picrite lava of the Emeishan large province, SW China.

American Mineralogist, 91, 1178–1183.

Zhao, Y., Xue, C., Liu, S. A., Mathur, R., Symons, D. T., Ke, J., Zhao, X.B., Seltmann, R., Jiao, J.G., Huang, Y.S., Wang, X.F. (2023) Vapor-phases as Cu transport agents for the shear-zone-hosted mineralization system: A perspective from H-O-S-Cu isotope. American Mineralogist, https://doi.org/10.2138/am-2022-8888.

Zhao, Y., Xue, C., Liu, S.A., Symons, D.T.A., Zhao, X., Yang, Y., and Ke, J. (2017) Copper isotope fractionation during sulfide-magma differentiation in the Tulaergen magmatic Ni–Cu deposit, NW China. Lithos, 286–287, 206–215.

Zheng, Y.C., Liu, S.A., Wu, C. Da, Griffin, W.L., Li, Z.Q., Xu, B., Yang, Z.M., Hou, Z.Q., and O'Reilly, S.Y. (2019) Cu isotopes reveal initial Cu enrichment in sources of giant porphyry deposits in a collisional setting. Geology, 47, 135–138.

Zhu, X.K., Guo, Y., Williams, R.J.P., O'Nions, R.K., Matthews, A., Belshaw, N.S., Canters, G.W., de Waal, E.C., Weser, U., Burgess, B.K., and others (2002) Mass fractionation processes of transition metal isotopes. Earth and Planetary Science Letters, 200, 47–62.

Zhu, X.K., O'Nions, R.K., Guo, Y., Belshaw, N.S., and Rickard, D. (2000) Determination of natural Cu-isotope variation by plasma-source mass spectrometry: Implications for use as geochemical tracers. Chemical Geology, 163, 139–149.

This is the peer-reviewed, final accepted version for American Mineralogist, published by the Mineralogical Society of America.
The published version is subject to change. Cite as Authors (Year) Title. American Mineralogist, in press.
DOI: https://doi.org/10.2138/am-2023-9155. http://www.minsocam.org/

Table 1 Experimental setups and conditions

No.	Capsule Material	T (°C)	P (MPa)	Time (hrs)	System	Cooling rate (K s^{-1})	pH
Set 1							
Cp15	Teflon	25	0.1	1	$Cu_{(f)}$ +1m HCl	n.m.	n.m.
Cp18	Teflon	25	0.1	1	$Cu_2O_{(P)}$+1m HCl	n.m.	n.m.
Cp16	Teflon	50	0.1	1	$Cu_{(f)}$ +1m HCl	n.m.	n.m.
Cp19	Teflon	50	0.1	1	$Cu_2O_{(P)}$+1m HCl	n.m.	n.m.
DQ180	Au	200	275	42	$Cu_{(s)}$+1.5 m HCl	0.5	0.19±0.02
Cp2	Au	300	100	24	$Cu_2O_{(P)}$+1.5m HCl	3	n.m.
DQ63	Cu	800	200	24	1.5 m HCl	3	4.87±0.53
DQ169*	Cu	800	200	144	Cu+$Cu_2O_{(s)}$+1.5m HCl+Qz	25	4.06±0.17
Set 2							
DQ175	Au	600	150	0.17	$Cu_{(s)}$+1.49 m NaCl	3	5.52±0.48
DQ173	Au	600	150	1	$Cu_{(s)}$+1.49 m NaCl	3	5.60±0.08
DQ174	Au	600	150	10	$Cu_{(s)}$+1.49 m NaCl	3	5.59±0.12
DQ172	Au	600	150	96	$Cu_{(s)}$+1.49 m NaCl	3	5.72±0.39
DQ178	Au	600	178	21	$Cu_{(s)}$+1.5m HCl	3	0.26±0.01
Set 3							
Cp3	Au	200	20	48	$Cu_2O_{(p)}$+0.90 m NaCl+pH buffer	ca.100	5.13±0.01
		200	20	48		ca.100	5.04±0.04
		100	20	50		0.014	5.06±0.01
		100	20	50		0.014	5.09±0.05
Cp4	Au	200	20	1	$Cu_2O_{(p)}$+0.90 m NaCl+pH buffer	25	4.68±0.01
Cp5	Au	200	20	48	$Cu_2O_{(p)}$+0.90 m NaCl+pH buffer	25	4.66±0.06
Cp6	Au	100	20	2	$Cu_2O_{(p)}$+0.90 m NaCl+pH buffer	ca.100	5.48±0.09
		150	20	3		ca.100	
		200	20	4		ca.100	
		250	20	6		ca.100	
		250	20	69		ca.100	

		150	20	71		0.014	5.42±0.12
Cp7	Au	250	20	48	$Cu_2O_{(p)}$+0.90 m NaCl+pH buffer	25	n.m.
Cp8	Au	250	20	48	$Cu_2O_{(p)}$+0.90 m NaCl+pH buffer	25	n.m.

Notes:

$Cu_{(f)}$, $Cu_{(s)}$, Cu(Au), $Cu_2O_{(s)}$ and $Cu_2O_{(P)}$ denotes Cu foil, Cu powder, Cu thin film coating Au substrate, cuprite powder and cuprite pellet, respectively.

pH values are determined by a microelectrode at room temperature, and the uncertainties are 95% confidences limit about the mean. pH buffer denotes 0.2 m $Na(CH_3COO)$/ CH_3COOH and the starting pH buffered NaCl solution has a pH value of 4.68±0.04.

Details of cooling rates are reported elsewhere in Qi et al. (2020).

n.m. = not measured

Table 2 Compositions of cuprite and its solid deposits determined by EPMA

No.	Cl wt%	Cu_2O wt%	Total wt%	mineral
Cuprite pellet				
Cp2	0.09	99.72	100.03	Cuprite
Cp3	0.02	100.12	100.26	Cuprite
Cp4	0.01	100.75	100.80	Cuprite
Cp5	0.01	99.44	99.49	Cuprite
Cp6	0.01	100.06	100.11	Cuprite
Cp7	0.00	99.69	99.95	Cuprite
Cp8	0.00	99.69	99.95	Cuprite
Solids on cuprite				
Cp2-S1	17.83	36.71	55.43	$CuCl{\cdot}nH_2O$
Cp2-S1	17.75	36.89	54.73	$CuCl{\cdot}nH_2O$
Cp2-S2	3.21	81.33	84.64	Hydrous Cu(II)
Cp2-S2	1.69	87.18	88.89	Hydrous Cu(II)
Cp2-S2	2.71	81.96	84.69	Hydrous Cu(II)
Cp4-S2	0.13	60.81	61.92	Hydrous Cu(II)
Cp4-S2	0.14	56.88	57.65	Hydrous Cu(II)
Cp5-S2	7.60	25.01	33.44	Hydrous Cu(II)
Cp5-S2	6.39	21.89	28.99	Hydrous Cu(II)
Cp5-S2	7.59	24.30	32.45	Hydrous Cu(II)

Notes: Sample number corresponds to the cuprite pellets and the experiments in which they were used, e.g., Cp2-S1 is a solid phase replacing cuprite pellet of Cp2, from experiment Cp2 (Table 1). S1 and S2 refer to S1 and S2 (see text for details).

This is the peer-reviewed, final accepted version for American Mineralogist, published by the Mineralogical Society of America.
The published version is subject to change. Cite as Authors (Year) Title. American Mineralogist, in press.
DOI: https://doi.org/10.2138/am-2023-9155. http://www.minsocam.org/

Table 3 Cu content and its isotopic composition of initial materials, fluids and solid products

SNO	T (°C)	Cu content (μg g^{-1})			Cu isotope composition (δ^{65}Cu, ‰)						
		Quench fluid	1st i.s. fluid	2nd i.s. fluid	Initial Cu/Cu_2O	Quench fluid	1st i.s. fluid	2nd i.s. fluid	S0	S1	S2
Set 1											
Cp15	25	1026			-0.41±0.05	-0.29±0.02					
Cp18	25	5753			0.43±0.02	0.95±0.03					
Cp16	50	1534			-0.41±0.05	-0.34±0.00					
Cp19	50	10727			0.43±0.02	1.32±0.01					
DQ180	200	13159			0.37±0.01	0.07±0.03					0.14±0.01
Cp2	300	538			0.51±0.02	1.10±0.02			0.23±0.01	0.23±0.04	1.26±0.02
DQ63	800	n.m.			0.02±0.02	0.49±0.01					
DQ169	800	5627	64409		0.47±0.02	0.05±0.02				0.09±0.02	
Set 2											
DQ175	600	16			0.37±0.01	0.79±0.02			1.20±0.01		0.75±0.02
DQ173	600	39			0.37±0.01	1.00±0.02			1.36±0.01		
DQ174	600	47			0.37±0.01	2.90±0.02			3.67±0.01		
DQ172	600	22			0.37±0.01	5.45±0.02			4.47±0.02		
DQ178	600	21769			0.37±0.01	2.37±0.02			2.74±0.01		
Set 3											
Cp3	200	n.m.	1510	1708	0.46±0.02	0.42±0.02*	0.46±0.04	0.43±0.02			
	100		2154	2846			0.57±0.02	0.35±0.01			
Cp4	200	722			0.46±0.03	1.41±0.01					-0.26±0.02
Cp5	200	712			0.48±0.04	1.32±0.03					0.23±0.32
Cp6	100	803*	879	832	0.42±0.04	0.13±0.01*	0.12±0.05	-0.10±0.03	0.39±0.02		
	150		969	1631			-0.06±0.02	-0.13±0.01			
	200		2442	2615			-0.02±0.05	0.01±0.02			
	250		3782	3756			0.08±0.04	0.15±0.01			
	250		735	2865			0.51±0.03	0.55±0.02			
	150		916	3160			0.50±0.03	0.52±0.01			
Cp7	250	1210			0.42±0.04	0.51±0.01			0.35±0.05		

Cp8	250	2673	0.48±0.04	0.55±0.01	0.32±0.02

Notes:

Cu content of 1st i.s. fluid of DQ169 is take from the measured Cu of synthetic fluid inclusions in the study of Qi et al.(2020).

* refers to Cu content of residual solution of Cp6. Extracted solutions of Cp6 after 69 h suffer a pressure medium dilution, and hence Cu content shown in this table has been corrected based the dilution factor.

Cu contents of solutions are determined by ICP-OES, and the uncertainties are better than 10% (2SD).

Solution nebulized MC-ICPMS has been used to determine the isotope composition of fluids, quench fluid precipitates and Cu on Au substrate, in situ LA-MC-ICPMS has been used to determine the isotope composition of initial Cu, Cu_2O and solids precipitated on cuprite pellet. The uncertainties of Cu isotope data are given by the two-sigma errors of the triplicated analyses.

Figure 1. Schematic drawings of experimental setups. (a) Set 1 experiments were conducted in Teflon vials with starting materials Cu_2O/Cu and HCl solution. (b) Experiments of sets 2, and 3 were performed in CSPVs with Cu/Au capsule which was loaded with Cu-bearing minerals and Cl-bearing solutions (modified after Qi et al., 2020). (c) A large volume fluid reactor (ref. Qi, 2019) was used in set 3 experiments. Au bag was loaded with Cu_2O and pH-buffered NaCl solution.

Figure 2. BSE images of cuprite after reaction (a-f) and photos of Au foils (g-l). a, c, d, e, f-Cross sections of cuprite pellets of Cp2, 4, 5; b-surficial area of Cp2. Note that a-c and d-e belong to Cp2 and Cp4 cuprite, respectively. g-Au foil before experiment; h-l—Au foils after Cu-NaCl/HCl reactions at 0.17, 1, 10, 21, and 96 h.

Figure 3. Cu content of quench fluids of Set 1 (a). Cu isotope fractionation between products (solution or solids) and initial Cu_2O (b). S1 and S2 refer to quench fluid precipitates and solid deposits on Cu_2O, respectively. Note that fluids are collected at room temperature and the abscissa (T) refers to the experimental temperature (in Celsius). The trendline in (a) excludes one point at 300℃ due to solids precipitation.

Figure 4. (a) Cu content variations (a) and its isotope fractionation between the fluids and native Cu (b) in Set 2. Runs are added with Cu + 8wt% NaCl, 600℃, 150 MPa, duration of 0.17−96 h.

Figure 5. Cu contents and its isotope fractionations in Set 3. Runs were added with Cu_2O + 5wt% NaCl + pH buffer, 200−250℃, 20 MPa, duration of 48−72 h. Runs (Cp3, 4, 5) were conducted at 200℃, 20 MPa for 48 h. In situ fluids of Cp3 were sampled at 200℃ and 100℃ during cooling with a rate of 0.0014 K/s. Cp6 was performed with increasing temperature from 100℃ to 250℃ and decreasing from 250℃ to 150℃. In situ fluids were sampled at a rate of 50℃/h during heating and cooling. Note that a second fluid sample was extracted at 250℃ before cooling. A drop of ca.1000 μg/g Cu of the second (69 h) in comparison to the first (5.5) one is likely due to acetate decomposition into CO_2 and CH_4 at 250℃. Thus, Cu partitions differently into fluid and gas phases.

Figure 6. Cu-O-H-Cl phase diagram at 25−600℃, 0.1-150 MPa. (a) C_{Cu}=0.016 m, C_{Cl}=1 m, 25℃, 0.1 MPa (Set 1-Cp15); (b) C_{Cu}=0.169 m, C_{Cl}=1 m, 50℃, 0.1 MPa (Set 1-Cp19); (c) C_{Cu}=0.045 m, C_{Cl}=0.9

m, 250°C, 20 MPa (Set 3-Cp6); (d) C_{Cu}=0.001 m, C_{Cl}=1.49 m, 600°C, 150 MPa (Set 2-DQ174).

Figure 7. $\Delta^{65}Cu$ values as a function of temperature. Reduction-induced fractionations are from Zhu et al. (2002), Ehrlich et al. (2004), Pękala et al. (2011), and Qi et al. (2019), $\Delta^{65}Cu_{fluid\text{-}Cu(I)}$ values related to Cu(I) sulfide oxidative leaching are from Mathur et al. (2005) and Kimball et al. (2009). The brown line represents the predicted equilibrium fractionation between Cu and $CuCl_2^-{}_{(aq)}$. At equilibrium $\Delta^{65}Cu_{Cu\text{ - }CuCl2^-(aq)} = 1000 \cdot \ln\beta_{Cu} - 1000 \ln\beta_{CuCl2^-}$, where β refers to the reduced partition function ratio (β_{Cu} and β_{CuCl2^-} are taken from Liu et al. (2021) and Sherman (2013), respectively). The blue line refers to the $\Delta^{65}Cu \propto T$ correlation derived from Ehrlich et al. (2004) and Qi et al. (2019), and this trend is extrapolated to 300 °C.

Figure 1

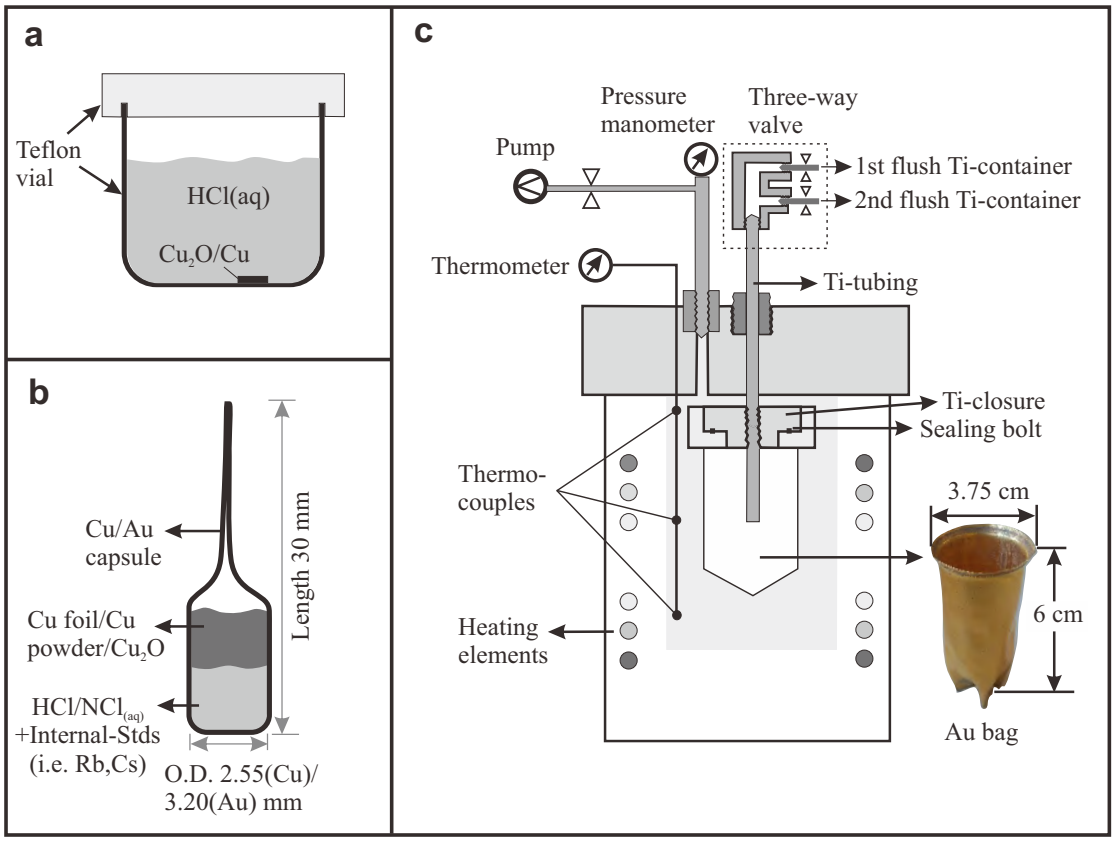

This is the peer-reviewed, final accepted version for American Mineralogist, published by the Mineralogical Society of America.
The published version is subject to change. Cite as Authors (Year) Title. American Mineralogist, in press.
DOI: https://doi.org/10.2138/am-2023-9155. http://www.minsocam.org/

Figure 2

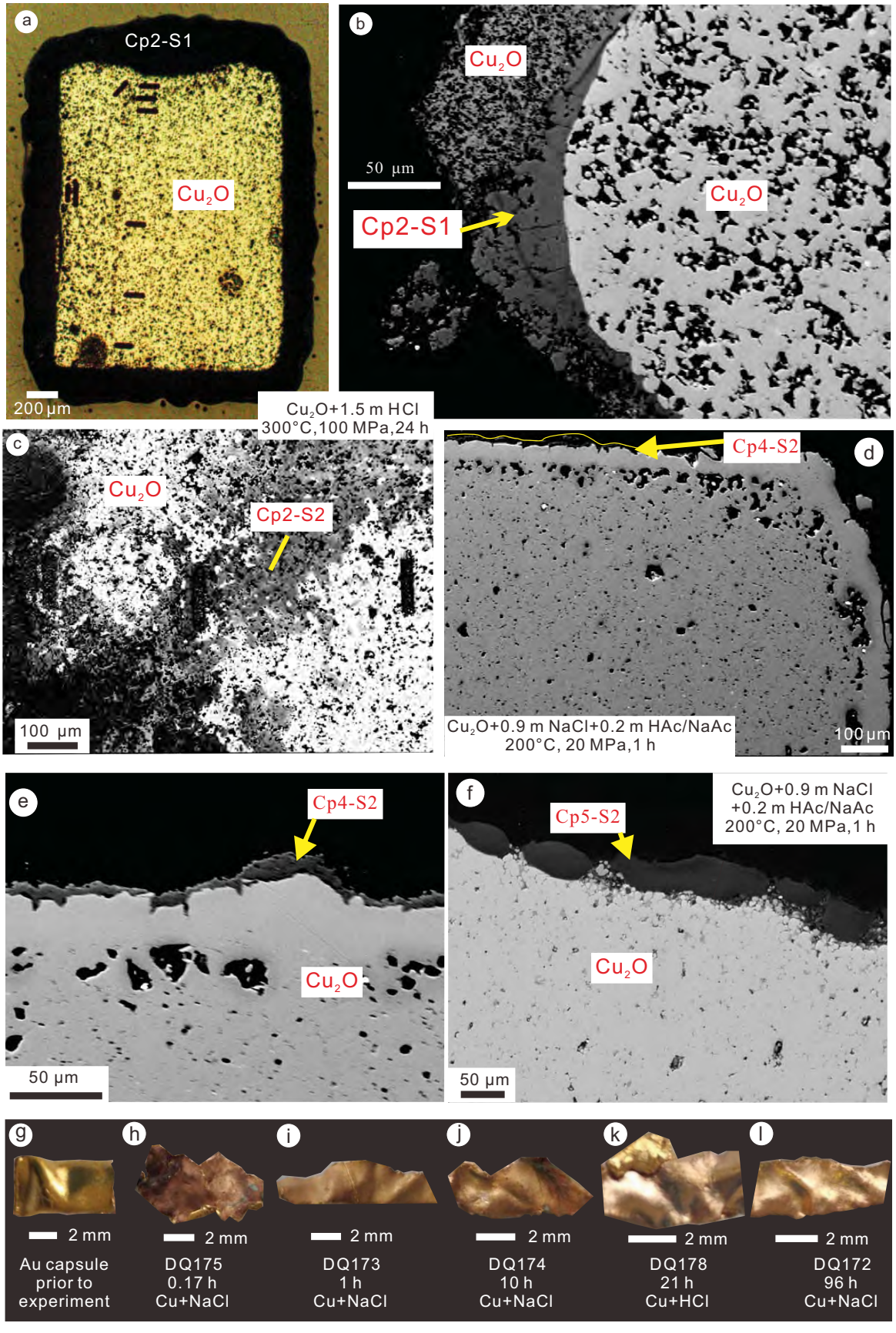

This is the peer-reviewed, final accepted version for American Mineralogist, published by the Mineralogical Society of America.
The published version is subject to change. Cite as Authors (Year) Title. American Mineralogist, in press.
DOI: https://doi.org/10.2138/am-2023-9155. http://www.minsocam.org/

Figure 3

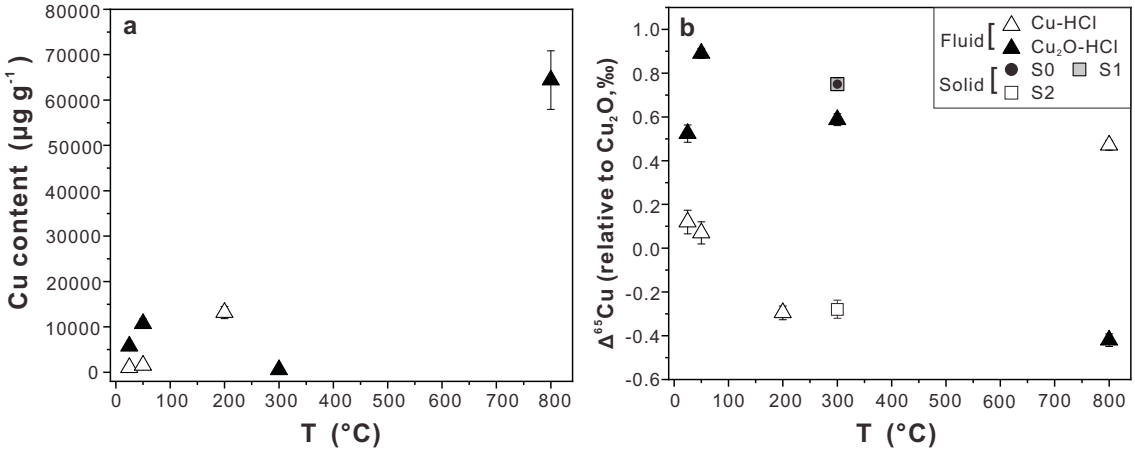

This is the peer-reviewed, final accepted version for American Mineralogist, published by the Mineralogical Society of America.
The published version is subject to change. Cite as Authors (Year) Title. American Mineralogist, in press.
DOI: https://doi.org/10.2138/am-2023-9155. http://www.minsocam.org/

Figure 4

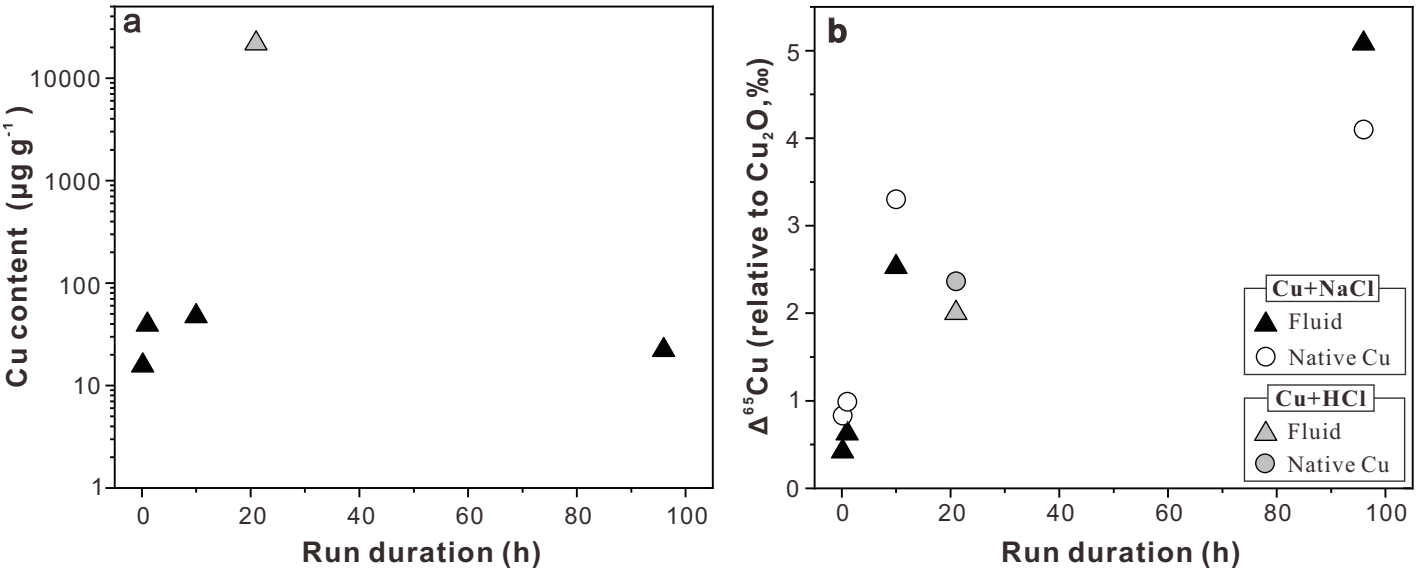

This is the peer-reviewed, final accepted version for American Mineralogist, published by the Mineralogical Society of America.
The published version is subject to change. Cite as Authors (Year) Title. American Mineralogist, in press.
DOI: https://doi.org/10.2138/am-2023-9155. http://www.minsocam.org/

Figure 5

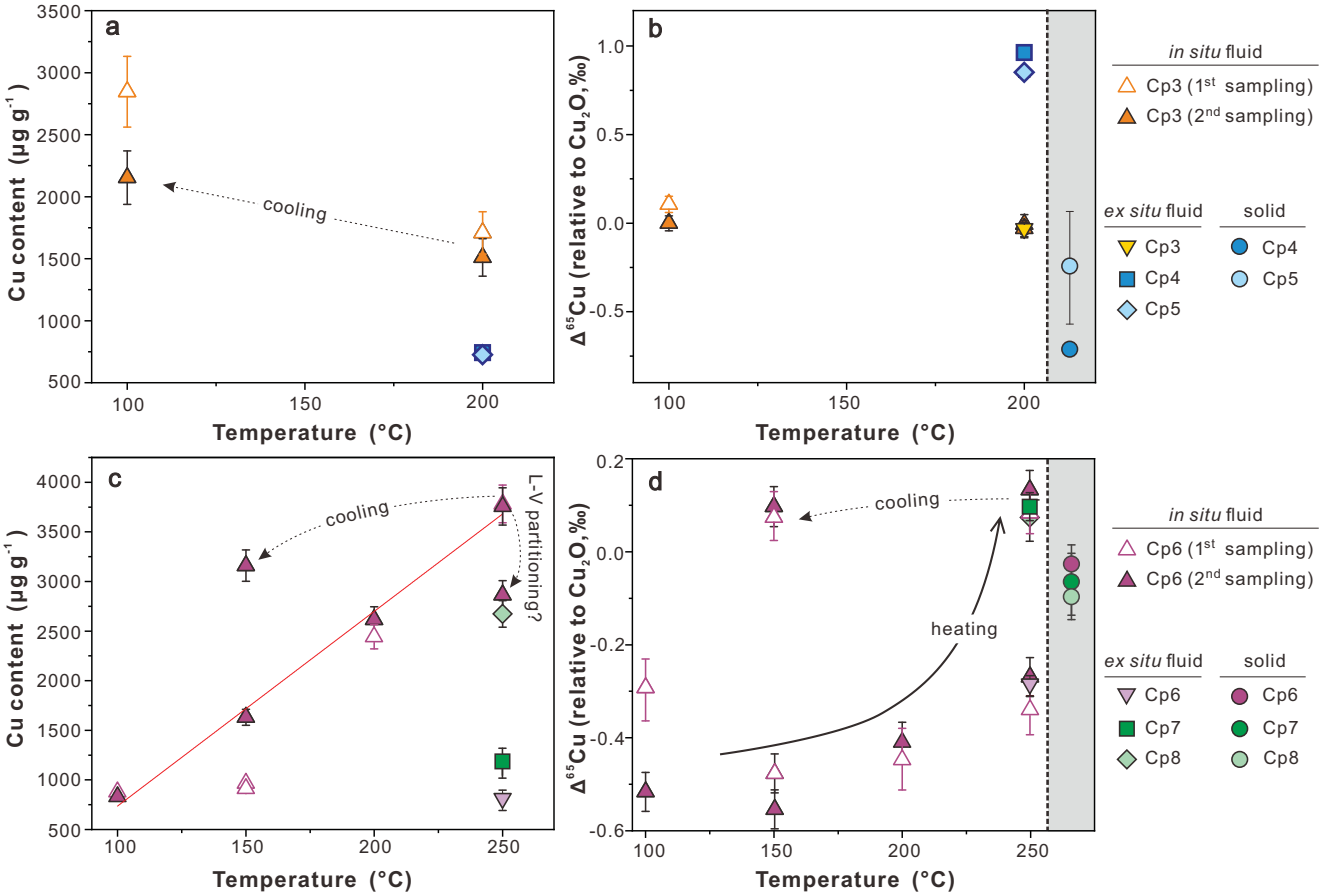

This is the peer-reviewed, final accepted version for American Mineralogist, published by the Mineralogical Society of America.
The published version is subject to change. Cite as Authors (Year) Title. American Mineralogist, in press.
DOI: https://doi.org/10.2138/am-2023-9155. http://www.minsocam.org/

Figure 6

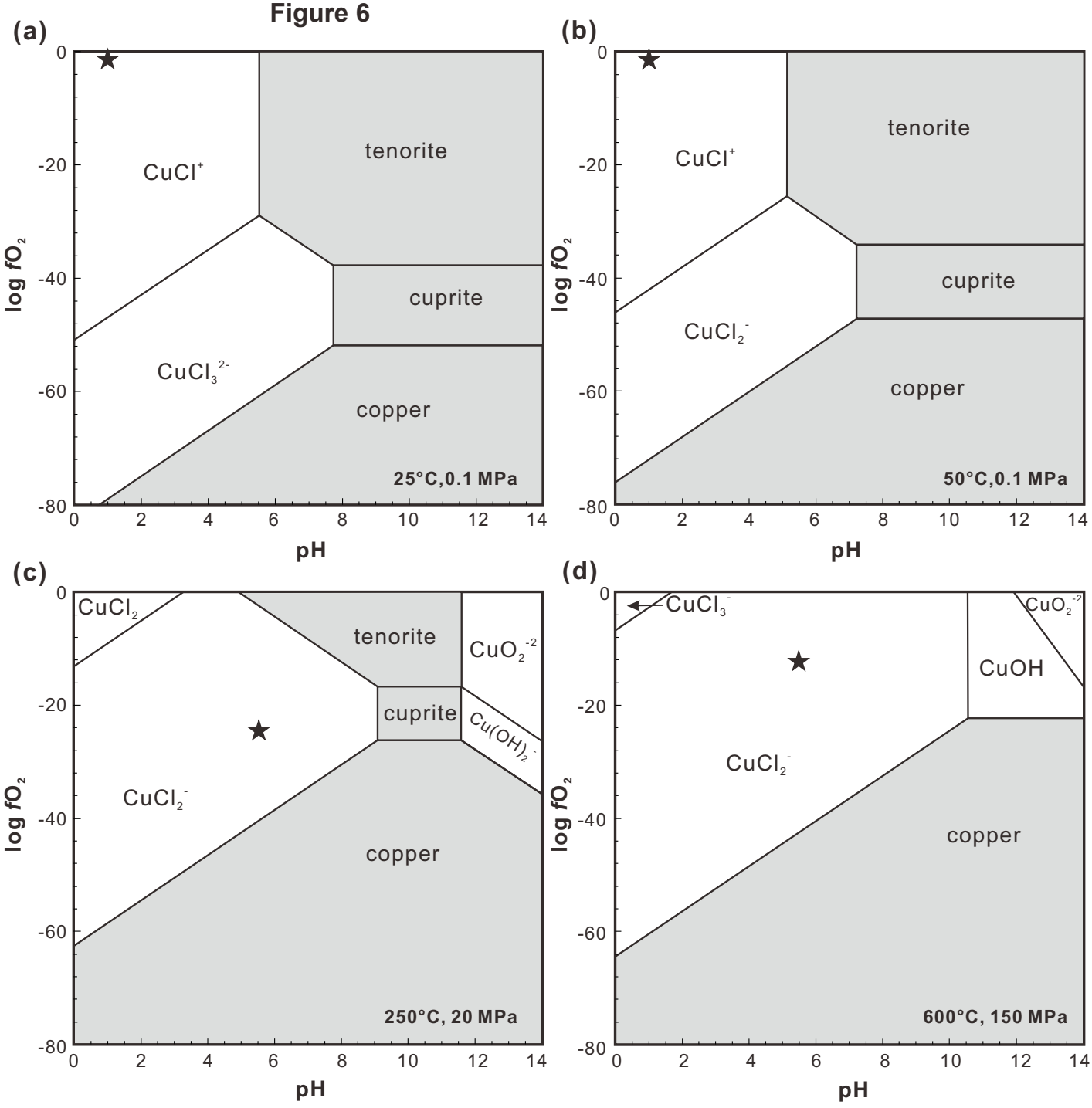

This is the peer-reviewed, final accepted version for American Mineralogist, published by the Mineralogical Society of America.
The published version is subject to change. Cite as Authors (Year) Title. American Mineralogist, in press.
DOI: https://doi.org/10.2138/am-2023-9155. http://www.minsocam.org/

Figure 7